SIAM J. APPL. MATH.
Vol. 80, No. 2, pp. 1003–1033

MODELING MICROSILICA PARTICLE FORMATION AND GROWTH DUE TO THE COMBUSTION REACTION OF SILICON MONOXIDE WITH OXYGEN*

RAQUEL GONZÁLEZ-FARIÑA†, ANDREAS MÜNCH†, JAMES M. OLIVER†, AND ROBERT A. VAN GORDER‡

Abstract. Microsilica particles arise as a byproduct of silicon furnace operation, created inside high temperature flames due to the combustion reaction of silicon monoxide with oxygen. These nanoparticles, which grow as silicon dioxide vapor condenses on the surface of existing particles, are used in a variety of composite materials. The size and quality of the particles affect the performance of the material used for such applications, and hence control of these quantities is of importance to manufacturers. Motivated by this, we derive a mathematical model that connects local thermal and chemical concentrations conditions to the formation and growth of microsilica particles. We consider two distinct reductions of our general model: the case of initially well-mixed or spatially homogeneous chemical species (modeling the region within the flame or reaction zone), and the case of initially spatially separated chemical species, in which diffusion will play a dominant role in providing material to a combustion front (modeling a larger cross section, which contains a reaction zone with limiting quantities of fuel which must diffuse into the reaction zone). In both cases, we provide asymptotic solutions for the temperature, chemical concentrations, and number density function of microsilica particles in the oxygen rich limit, and compare them to numerical simulations. Motivated by realistic furnace control mechanisms, we treat the relative quantity of oxygen to other fuel components and the saturation concentration of silicon dioxide as control parameters, discussing how each may be used to modify the properties (such as size and abundance) of microsilica particles formed. One physically interesting finding is the theoretical description of a bimodal distribution for microsilica particle size which was previously observed in experiments.

Key words. particle growth, reaction-diffusion systems, asymptotic analysis, moment equations, microsilica, silica fume

AMS subject classifications. 35Q79, 35C20, 35Q70, 80A32, 80M35

DOI. 10.1137/19M1287080

1. Introduction.

Microsilica or silica fume is a byproduct of the silicon and ferrosilicon industry. It consists mainly of spherical particles of amorphous SiO_2 with more than 95% of them being finer than $1\mu m$ [31] (see Figure 1). These particles mainly grow by condensation but can also form aggregates and agglomerates as discussed below. The primary industrial use of microsilica is as an additive in high performance concrete, but it is also utilized for refractories and polymers. Modifications in the silicon production process affect not only the microsilica yield but also the quality and properties of the particle. Depending on the application, certain particle sizes or surface areas are preferred [10], and as such, there is a need to study which conditions are favorable for microsilica formation and growth.

*Received by the editors September 13, 2019; accepted for publication (in revised form) February 27, 2020; published electronically April 27, 2020.
https://doi.org/10.1137/19M1287080
Funding: This work was supported by the EPSRC Center for Doctoral Training in Industrially Focused Mathematical Modelling through grant EP/L015803/1 in collaboration with Elkem.

†Mathematical Institute, University of Oxford, Andrew Wiles Building, Radcliffe Observatory Quarter, Woodstock Road, Oxford, OX2 6GG, United Kingdom (gonzalezfari@maths.ox.ac.uk, muench@maths.ox.ac.uk, oliver@maths.ox.ac.uk).
‡Department of Mathematics and Statistics, University of Otago, P.O. Box 56, Dunedin 9054, New Zealand (rvangorder@maths.otago.ac.nz).

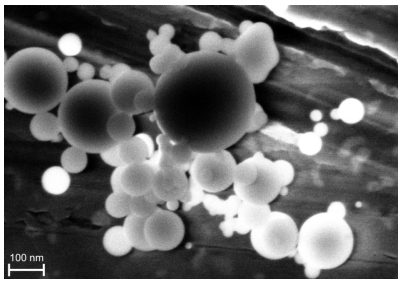

FIG. 1. *SEM image of microsilica particles (provided by Elkem). The majority of the particles are perfectly spherical and form agglomerates (weak bonds), while a small percentage form aggregates (some with irregular shape as in the top right corner).*

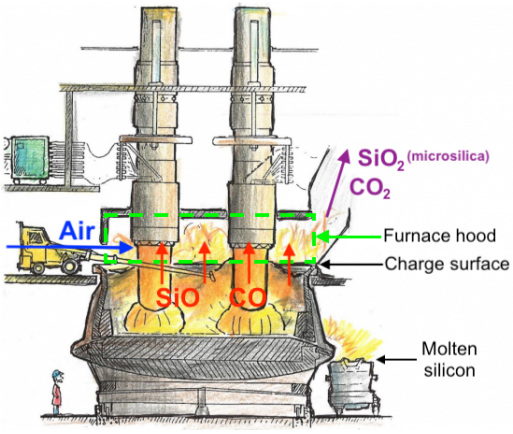

FIG. 2. *Sketch of a silicon furnace indicating the location of the furnace hood (green dashed square), that is, where the combustion reactions* (1) *happen. Reproduced from* The Si Process Drawings, *by Thorsteinn Hannesson.*

Microsilica particles are formed inside high temperature flames due to the combustion of SiO gas with oxygen, which is a byproduct of the quartz reduction process to obtain silicon. Another byproduct of the process is CO gas which also combusts, producing less bright and thus less hot flames. Therefore, both chemicals, SiO and CO, compete for oxygen. In Figure 2, we provide a sketch of an industrial silicon furnace where both silicon and microsilica are produced (refer to [31, 35] for more details on the silicon manufacturing process). In some configurations, the oxygen is provided via air which enters the furnace hood through side doors, and hence the quantity of oxygen can be controlled. We focus our attention on the two exothermic combustion reactions happening in the furnace hood, namely

$$2\mathrm{SiO(g)} + \mathrm{O_2(g)} \xrightarrow{R_1} 2\mathrm{SiO_2(g)} \quad \text{and} \quad 2\mathrm{CO(g)} + \mathrm{O_2(g)} \xrightarrow{R_2} 2\mathrm{CO_2(g)}. \tag{1}$$

Before the particles form, SiO_2 is in a vapor phase, which can be treated as an ideal gas. When this vapor reaches saturation, it undergoes a change of state from gas into solid that also releases energy and under which the particles form. After nucleation, the growth of the primary particles is purely by condensation, that is, by molecular addition of mass to the surface of existing particles, which is the main focus of this paper. Additionally, some small percentage of the primary particles created show

aggregation, like the one attached to the top of the largest particle in Figure 1 with an irregular shape. In later stages of the process, when microsilica is collected, a high percentage of particles agglomerate via weak interparticle forces, as can be seen from Figure 1, where most particles are attached to each other. Since aggregation does not occur frequently, and agglomeration at late stages is not very relevant to industrial scale production (since the weak bonds can be broken easily with a dispersing machine [10]), we will not study these mechanisms in this work and will only focus on the formation and growth of the primary particles through condensation.

Several mathematical models [14, 22, 34, 35] have been developed for the heat and mass balances, chemical reactions, and thermodynamics within silicon furnaces. These models may be used to predict the behavior of the furnace below the charge surface where the reduction of quartz occurs, resulting in molten silicon which then exits the furnace, is collected, and solidifies into usable product [6]. Far less attention has been focused on modeling processes inside the combustion chamber which lead to the creation of microsilica, yet this too is of industrial use. In [17], NO formation is considered at different parts of the silicon process (in the absence of chemical reactions), which is strongly correlated to the formation of silica fume. A similar model is introduced in [16] which is also coupled to chemical reactions due to the combustion of the off-gases; however, this model captures the dynamics of taphole gases during the tapping of the silicon, which is slightly different from the physics and chemistry involved in a furnace hood.

Although the application is different, literature on the formation and growth of aerosol particles will be useful in motivating aspects of our model. When studying aerosols, a common approach is to use population balance equations to model physical mechanisms including nucleation, continuous growth, coagulation, and breakage within a population of particles with different sizes [30], in order to predict particle size distribution and other properties. Flagan and Lunden [12] considered growth of nanoparticles by coagulation and coalescence from the vapor phase, giving expressions for the Brownian collision rates for both spherical particles and complex agglomerate structures. Pratsinis [28] considered a model for simultaneous nucleation, condensation, and coagulation in aerosol reactors, in terms of the moments of the aerosol size distribution. Surface reaction is another common growth mechanism, and Artelt, Schmid, and Peukert [3] studied the formation and growth of titania particles from the vapor phase, concluding that reaction on the surface of existing TiO_2 is the dominant growth mechanism. Similar studies on nucleation and growth of fine particles have been undertaken for MgO smoke [37] and microalumina particles [4]; the latter explores how the condensation reaction depends on thermal effects by deriving equations for the number density of each reacting species and for the temperature. We adopt this approach for our model, focusing on the continuous growth of the particles by condensation as the growth mechanism. There exist population balance models in the literature for the formation of silica particles from the gas phase [19, 32, 33], yet in these cases silica particles are generated under different conditions than the ones in this study and therefore their properties, formation, and growth mechanisms are slightly different.

Existing models for particle formation via combustion use simplified profiles and equations for the chemicals and temperature variations in the combustion chamber, leading to chemical models which are uncoupled or one way coupled with the particle growth mechanism. In this work, we present a fully coupled system that includes the effects of the chemical concentrations and temperature differences on the particles, and vice versa. Motivated by studies carried out on heat and mass balances, chemical

reactions, and thermodynamics within silicon furnaces [34, 35], we couple a model that predicts the local temperature profiles and chemistry within the furnace hood to the population balance equation through the growth and nucleation rates. We couple the population balance equation back into the temperature and concentration of the condensed material within the furnace through source and sink terms similar to those used in [1, 23].

The remainder of this paper is organized as follows. In section 2 we develop the mathematical model and present a nondimensional version of it under the assumption of a simplified geometry. While there are a number of parameters in our model, most are well known, with the initial concentration of oxygen and saturation concentration of silicon dioxide being the two free parameters which we may control. In section 3 we study the well-mixed limit for all chemical species, which is a caricature of the zoomed in region within the combustion or reaction zone. In section 4 we consider the scenario where oxygen is initially spatially segregated from the other chemical species, with a reaction boundary forming between the two. In order to gain a qualitative understanding of the heat and mass transfer problem, we obtain asymptotic solutions for both reductions of our model for an oxygen rich environment and in the limit where the feedback of particle growth on temperature and chemistry is small, while we consider numerical simulations for more general parameter regimes. We discuss our results and their relevance to industrial scale production of microsilica in section 5.

2. Mathematical model. We are interested in modeling the dynamics of the main chemical species found in the furnace hood above the charge surface: $N_2(g)$, $O_2(g)$, $SiO(g)$, $SiO_2(g)$, $CO(g)$, and $CO_2(g)$. Other compounds such as volatiles are not taken into account. Thus, we model the fluid as a combination of the gaseous species mentioned before, where the only chemical reactions occurring are the combustion reactions (1). We consider equations for the conservation of mass and energy coupled to a particle growth model, while greatly simplifying the flow problem by choosing the velocity of the fluid to be uniform in space and time on an unbounded spatial domain. For such a configuration, the velocity can be scaled out with a change of space variable moving with the flow. Subsequent work will consider more realistic flow regimes, but for now these assumptions are sufficient to study the regions local to a reaction zone where the microsilica is produced, as is the focus of this paper.

2.1. Conservation of chemical species. The mass conservation equations express how the concentration of each species depends on the diffusion of species and chemical reactions. Taking $C_X(\mathbf{x}, t)$ to be the concentration of species X in units $\mathrm{mol/m^3}$, where $\mathbf{x}$ denotes position in cartesian coordinates and t time, the governing equations are given by

$$\frac{\partial C_{\mathrm{N_2}}}{\partial t} - D_{\mathrm{N_2}} \boldsymbol{\nabla}^2 C_{\mathrm{N_2}} = 0, \tag{2a}$$

$$\frac{\partial C_{\mathrm{O_2}}}{\partial t} - D_{\mathrm{O_2}} \boldsymbol{\nabla}^2 C_{\mathrm{O_2}} = -R_1 - R_2, \tag{2b}$$

$$\frac{\partial C_{\mathrm{SiO}}}{\partial t} - D_{\mathrm{SiO}} \boldsymbol{\nabla}^2 C_{\mathrm{SiO}} = -2R_1, \tag{2c}$$

$$\frac{\partial C_{\mathrm{SiO_2}}}{\partial t} - D_{\mathrm{SiO_2}} \boldsymbol{\nabla}^2 C_{\mathrm{SiO_2}} = 2R_1 - S_C, \tag{2d}$$

$$\frac{\partial C_{\mathrm{CO}}}{\partial t} - D_{\mathrm{CO}} \boldsymbol{\nabla}^2 C_{\mathrm{CO}} = -2R_2, \tag{2e}$$

$$\frac{\partial C_{\mathrm{CO_2}}}{\partial t} - D_{\mathrm{CO_2}} \boldsymbol{\nabla}^2 C_{\mathrm{CO_2}} = 2R_2, \tag{2f}$$

where D_X is the diffusion rate of species X, R_i, $i = 1, 2$, are the source terms due to the combustion reactions given in (1), and S_C represents a sink term due to the formation of the particles which will be defined in section 2.4. We have included conservation of the two main components in air, N_2 and O_2, which appear to be in much higher concentrations than the rest of the species. In addition, SiO and CO are competing for the oxygen, while we assume the nitrogen to be nonreacting even though in some cases it could react with oxygen forming NO_x compounds. Here, we only consider the dominant reactions, but note that others could in principle be introduced to the model.

For elementary chemical reactions, the reaction rate is proportional to a power of the concentrations of the reactants according to the law of mass action. However, for more complex reactions simplified kinetic models are often adopted, where the powers may not be equal to the stochiometric coefficients of the reacting species and are often instead determined experimentally [7, 39, 43]. In our case, the combustion of SiO and CO with oxygen involves some intermediate chemical reactions that are not fully understood by our industrial partners. However, since the essential nature of the process is that SiO, CO, and oxygen are consumed while products and heat are generated, both combustion reactions are well approximated by one-step irreversible processes represented by (1). Here we consider each reaction to be first order in both reactants [11]. The reaction rates are typically highly dependent on the temperature and this is included by considering an Arrhenius term of the form $K_i(T) = A_i \exp(-E_i/RT)$, where E_i is the activation energy of the reaction, A_i is a preexponential coefficient, T is the temperature of the system, and $R = 8.314$ $\mathrm{J{\cdot}mol^{-1}K^{-1}}$ is the universal gas constant. Thus, we adopt the reaction rates given by $R_1 = K_1(T) C_{\mathrm{SiO}} C_{\mathrm{O_2}}$, $R_2 = K_2(T) C_{\mathrm{CO}} C_{\mathrm{O_2}}$. Notice that we can easily express the concentrations used above in terms of partial pressures (P_i) by using Dalton's law of partial pressures, namely $C_i = P_i C_T / P$, for every chemical species i, where P is the total pressure of the fluid, and $C_T = \sum_{\text{species } i} C_i$. A full list of the dimensional parameters used in our model is given in Table 1.

2.2. Conservation of energy. We now consider how the temperature, $T(\mathbf{x}, t)$, varies in space and time. The temperature is affected by the thermal conductivity of the fluid and by the heat released by the chemical reactions (S_R) and the change of state due to the formation of the particles (S_T). Thus, we have the conservation of energy equation

$$\frac{\partial}{\partial t}\left(\rho_0 c_p T\right) - \boldsymbol{\nabla} \cdot (\kappa \boldsymbol{\nabla} T) = S_R + S_T, \tag{3}$$

where ρ_0, c_p, and κ denote the fluid density, heat capacity, and thermal conductivity, and are assumed to be constant. The source term due to the chemical reactions is given by $S_R = \Delta H_1 R_1 + \Delta H_2 R_2$, where ΔH_i is the heat release of reaction i, and S_T is given in section 2.4.

2.3. Population balance equation. We consider the particle formation and growth mechanisms and introduce the population balance equation as the means to model them. We assume that we have a population of particles with different sizes growing at different rates that depend on the chemical species concentrations and

TABLE 1

Typical values of dimensional parameters used in the model. [1]*Estimated value obtained from* [11]. [2]*Stokes–Einstein theory approximates the diffusion coefficient of a particle of radius* r *by the relation* $D_p = \frac{k_B T_1}{6\pi\mu r}$, *where* k_B *is the Boltzman's constant.* [3]*Obtained from the software HSC Chemistry.* [4]*Since air is the dominant component in the fluid. At* $T = 1000$ *K and* $P = 1$ *atm.*

Parameter	Typical value	Units	Reference
$C_{O_2,0}$	$2 - 100$	mol/m^3	Input concentration of O_2[1]
$C_{SiO,0}$	1	mol/m^3	Input concentration of SiO[1]
$C_{CO,0}$	1	mol/m^3	Input concentration of CO[1]
A_1	1.0×10^7	m^3/(mol·s)	[17]
A_2	1.80×10^4	m^3/(mol·s)	[38]
T_1	1713	K	Temperature of the fuel [11]
T_2	1073	K	Temperature of the air [11]
D_{O_2}	4.7×10^{-4}	m^2/s	[25]
D_{SiO}	3.9×10^{-4}	m^2/s	[25]
D_{SiO_2}	3.9×10^{-4}	m^2/s	Taken to be the same as D_{SiO}
D_{CO}	1.804×10^{-5}	m^2/s	[24]
D_{CO_2}	1.429×10^{-5}	m^2/s	[24]
D_p	10^{-9}	m^2/s	Determined from Stokes-Einstein theory[2]
c_p	1005	J/(kg·K)	[17]
ΔH_1	3.930×10^5	J/mol	Enthalphy of SiO combustion[3]
ΔH_2	1.395×10^5	J/mol	Enthalphy of CO combustion[3]
E_1	27196	J/mol	[17]
E_2	9974.65	J/mol	[38]
R	8.314	J/(mol·K)	Universal gas constant
ρ_0	0.3529	kg/m^3	Density of air[4]
κ	5.784×10^{-2}	W/(m·K)	Thermal conductivity of air[4]
C_e	$0 - 1$	mol/m^3	Estimated
M	6.008×10^{-2}	kg/mol	Molar mass of SiO_2
m	9.96×10^{-26}	kg	Atomic mass of SiO_2
ρ_p	2196	kg/m^3	Density of SiO_2
$s_{\min}$	2×10^{-8}	m	Smallest particle seen in experiments[1]
J_0	10^{25}	1/(m^3· s)	[21]
v_C	4.536×10^{-29}	m^3	Volume of a molecule of SiO_2
γ	3.20×10^{-2}	J/m^2	[11]
k_B	1.3806×10^{-23}	J/K	Boltzman's constant
L_V	2.1930×10^{10}	J/m^3	[20]

temperature. Let dN be the number density of particles, that is, the number of particles per unit volume of gas, at a given spatial location $\mathbf{x}$, at a given time t, and with size in the range $[s, s + \mathrm{d}s]$, where we take the diameter of the particle to characterize the particle size. We write $dN = n(s, \mathbf{x}, t)\mathrm{d}s$, which defines the particle size distribution function or number density function $n(s, \mathbf{x}, t)$ [30].

The dominant microsilica particle growth mechanisms considered in our model are nucleation and condensation, the latter meaning surface growth by the deposition of monomers of SiO_2 on SiO_2 particles. Letting G be the growth rate due to condensation, the population balance equation has the form

$$\frac{\partial n}{\partial t} - D_p \boldsymbol{\nabla}^2 n + \frac{\partial}{\partial s}\left(G(\boldsymbol{x}, t)n - D_s \frac{\partial n}{\partial s}\right) = 0. \tag{4}$$

The particle-phase or molecular diffusivity, D_p, is usually negligible for fine particles in turbulent flames [29, 44]. The main reason is that particles do not diffuse with respect to the gas phase since their size is large compared to the gas-phase chemical species. However, the diffusion term may be retained in order to account for turbulent diffusivity [45]. We can also include diffusion in the size space (D_s) which represents fluctuations around G. Notice that this diffusion coefficient is dependent on G, and as an approximation it can be taken to be proportional to the growth rate [23]. Since the inclusion of D_s regularizes the PDE (4), it is often added when needed for stability of numerical solutions, though we set $D_s = 0$ throughout this work. In order to close the model we need to determine the form of the rate expressions for nucleation, J, which is built into the model via a boundary condition on (4), and for surface growth, G.

2.3.1. Nucleation rate. The nucleation rate of particles is included into the model as a boundary condition for the particle size coordinate (s) in the governing equation (4), by equating it to the "particle flux" in at $s = s_{\min}$ as in [30]: $n(s_{\min}, t)G(s_{\min}, t) = J$. We consider homogeneous nucleation as opposed to heterogeneous, meaning that the new thermodynamic phase forms spontaneously and randomly rather than at nucleation sites on surfaces. The rate at which nucleation of particles occurs is determined by the probability of forming the critical nucleus diameter. This is the diameter that maximizes the Gibbs free energy ($\Delta\mathcal{G}$), which corresponds to where the particle is at equilibrium with the surrounding vapor, and is given by $s_{\min} = 4\gamma v_C/(k_B T \ln S_e)$, where γ, v_c, and k_B are the surface energy, volume of a SiO_2 molecule, and the Boltzman's constant, respectively. The quantity $S_e = C_{SiO_2}/C_e$ denotes the saturation ratio, with C_e being the saturation or equilibrium concentration. Note that in some literature S_e will be defined as the ratio of partial pressures or vapor concentrations [27, 42, 44]. The value of C_e for SiO_2 may in general depend on a number of atmospheric variables and other considerations, as varying ranges are given for different applications [2, 18]. Since a proper value or range of C_e is not uniquely defined in the literature for our problem, we treat C_e as a parameter which may be varied from zero to one, and determine the sensitivity of solutions on this parameter.

The value $s_{\min}$ is the minimum size required for nucleation to occur. The corresponding nucleation rate is usually given according to classical nucleation theory [13, 44] as

$$J = J_0 \exp\left(-\frac{\Delta\mathcal{G}^*}{k_B T}\right) = J_0 \exp\left(-\frac{16\pi\gamma^3 v_C^2}{3(k_B T)^3 (\ln S_e)^2}\right), \tag{5}$$

where we can take the form of the nucleation rate coefficient J_0 from [44], although throughout this paper it will be considered to be a constant. Refer to [13, 41] for further details on the derivation of (5).

2.3.2. Growth rate. Consider a relatively small particle (diameter $< 1\mu m$) of pure species SiO_2 in air that also contains vapor molecules of SiO_2, growing due to vapor condensation. In our case, the mean free path of the gas surrounding the particle is large compared to the size of the growing particle itself (free-molecule regime) [36], thus classical kinetic theory is applied in order to determine the growth rate. We assume the particle to be spherical and do not take into account any interaction forces between the particle and vapor. The collision rate of the gas molecules hitting a unit area in unit time, also called the effusion flux, is given by $\mathcal{F} = N\bar{c}/4$, where N is the number concentration of molecules in the gas, and $\bar{c}$ is the mean molecular velocity. The mean velocity is obtained by finding the mean of the Maxwell–Boltzmann

distribution, and this is $\bar{c} = \sqrt{8k_BT/(\pi m)}$ where k_B is the Boltzman's constant and m is the atomic mass of SiO_2. Therefore, $\mathcal{F} = (C_{SiO_2} - C_e)\sqrt{8k_BT/(\pi m)}/4$. The rate of condensation, F, to the particle surface is obtained by multiplying the effusion flux by the surface area of the particle [13], giving

$$F = (C_{SiO_2} - C_e)\sqrt{\frac{k_BT}{2\pi m}}\pi s^2. \tag{6}$$

The rate of particle volume growth is then given by multiplying F by the ratio of SiO_2 molar mass to density so that the dimensions are consistent,

$$\frac{dv}{dt} = F\frac{M}{\rho_p} = \sqrt{\frac{k_BT}{2\pi m}}(C_{SiO_2} - C_e)\pi s^2\frac{M}{\rho_p}, \tag{7}$$

thus the diameter growth rate is

$$\bar{G} = \frac{ds}{dt} = \frac{2M}{\rho_p}\sqrt{\frac{k_BT}{2\pi m}}(C_{SiO_2} - C_e). \tag{8}$$

Since it is well known that microsilica particles do not shrink ($\bar{G} > 0$), in our model we will take

$$G = \bar{G}\mathcal{H}\left(C_{SiO_2} - C_e\right) \tag{9}$$

as the particle growth rate, where $\mathcal{H}$ represents the Heaviside function.

2.4. Coupling the particle growth and chemical reaction models. The particle formation and growth model is coupled to the chemical species concentrations and temperature directly via the growth rate for condensation, G, and the nucleation rate, J. These rates depend on the concentration of vapor silicon dioxide, C_{SiO_2}, predicted by (2d) and on the temperature of the system given by (3).

Moreover, in order to account for the material consumed and heat produced due to the formation of the particles, we add a sink term S_C (units $[\mathrm{mol}\cdot\mathrm{m}^{-3}\cdot\mathrm{s}^{-1}]$) in (2d) and a source term S_T (units $[\mathrm{J}\cdot\mathrm{m}^{-3}\cdot\mathrm{s}^{-1}]$) in (3). The form of these terms comes from integrating the mass flux through the surface of a spherical particle, F as in (6), times the particle density, n, over all particle diameters. That is,

$$S_C = \int_{s_{\min}}^{\infty} Fn\mathrm{d}s = \frac{\pi}{2}\frac{\rho_p}{M}G\int_{s_{\min}}^{\infty} s^2n\mathrm{d}s. \tag{10}$$

Since mass transfer is the driving mechanism for particle growth, the source term for the energy released due to the formation of the particles is proportional to (10). We simply multiply it by the enthalpy of formation of the particle, ΔH_p, which has physical units $[\mathrm{J}\cdot\mathrm{mol}^{-1}]$, or equivalently by $L_V\frac{M}{\rho_p}$, where L_V is the specific latent heat for condensation with units $[\mathrm{J}\cdot\mathrm{m}^{-3}]$. This is

$$S_T = \Delta H_p\int_{s_{\min}}^{\infty} Fn\mathrm{d}s = \frac{\pi}{2}L_VG\int_{s_{\min}}^{\infty} s^2n\mathrm{d}s. \tag{11}$$

2.5. Moments of the distribution. In practice, we can decouple the PDE for particle formation (4) from the system of ODEs that models the temperature and chemicals by including three extra ODEs for the zeroth, first, and second moments of the particle distribution n, in the following way. First note that the kth moment is given by $M_k = \int_{s_{\min}}^{\infty} s^k n \mathrm{d}s$, hence the integral part of the expressions derived for S_C and S_T in the previous section corresponds to M_2. Now, multiplying the PDE (4) (with $D_s = 0$) by s^k, for $k = 0, 1, 2$, and integrating each case with respect to s, we obtain the ODEs

$$\frac{\mathrm{d}M_0}{\mathrm{d}t} - D_p \boldsymbol{\nabla}^2 M_0 = J, \tag{12a}$$

$$\frac{\mathrm{d}M_1}{\mathrm{d}t} - D_p \boldsymbol{\nabla}^2 M_1 = s_{\min} J + G M_0, \tag{12b}$$

$$\frac{\mathrm{d}M_2}{\mathrm{d}t} - D_p \boldsymbol{\nabla}^2 M_2 = (s_{\min})^2 J + 2 G M_1. \tag{12c}$$

Therefore, we can solve the latter three equations altogether with the concentrations and temperature model, and separately from the equation for n which is slightly more challenging due to the extra dimension. A similar approach has been considered elsewhere [27, 42] for solving related population balance models in terms of moments.

2.6. Nondimensional model for a simplified geometry. From the form of the reaction kinetics, the conservation equation for N_2 decouples from the others, and we do not include it in our model. We consider a simplified, one-dimensional geometry given by a cross section of the reaction zone or flame front, that is, $z \in (-\infty, \infty)$, where C_{O_2} is initially at maximal concentration as $z \to \infty$, whereas C_{SiO} and C_{CO} are initially at maximal concentration as $z \to -\infty$. Initial data will be prescribed based on the desired initial configuration, with either well-mixed or spatially partitioned initial profiles for the initial concentrations of chemicals and temperature. We shall assume a zero initial profile for the particle distribution as well as for the moments; there will be no particles already in the system at the initial time. Thus, the initial conditions can be written as $C_X = C_{X,\text{initial}}(z)$, $T = T_{\text{initial}}(z)$, $n = M_0 = M_1 = M_2 = 0$ at $t = 0$, where the form of the functions will be discussed later. We also have a boundary condition for n, $Gn = J$ at $s = s_{\min}$, with the dimensional particle growth, G, and nucleation, J, rates given by (9) and (5), respectively.

We nondimensionalize the equations previously defined by scaling the variables in the following way: $T = (T_1 - T_2)\tilde{T} + T_2$, where T_1 is the temperature of the fuel as it leaves the charge surface and T_2 is the temperature of the air coming from outside the furnace (in practice $T_2 < T_1$), $C_X = C_{X,0}\tilde{C}_X$, where $C_{X,0}$ represents the input concentration of the reactant X while for the products we take $C_{SiO_2,0} = C_{SiO,0}$ and $C_{CO_2,0} = C_{CO,0}$, $t = t_0\tilde{t}$, $z = z_0\tilde{z}$, $s = s_0\tilde{s}$, $n = n_0\tilde{n}$, and $M_i = m_i\tilde{M}_i$ for $i = 0, 1, 2$. We choose the timescale with the dominant reaction kinetics and the spatial scale is taken with the dominant diffusion D_{O_2}, namely

$$t_0 = \frac{1}{2A_1 C_{O_2,0}} \exp\left(\frac{E_1}{RT_1}\right), \quad z_0 = \sqrt{D_{O_2} t_0} = \sqrt{\frac{D_{O_2}}{2A_1 C_{O_2,0}}} \exp\left(\frac{E_1}{2RT_1}\right). \tag{13}$$

Additionally, we scale the particle diameter with the critical diameter for nucleation, $s_0 = s_{\min}$, the number density function with the ratio between nucleation and growth rate coefficients, $n_0 = J_0/G_0$ where $G_0 = 2MC_{SiO_2,0}\sqrt{k_B(T_1 - T_2)/(2\pi m)}/\rho_p = 6.5 \times 10^{-3}$, and the moments with a combination of the latter two scalings, $m_i = n_0 s_0^{i+1}$, $i = 0, 1, 2$. A full list of dimensionless parameter groups is given in Table 2.

TABLE 2

Definitions and typical values for nondimensional parameters used in the model. We treat a and C_{sat} as control parameters, whereas the other parameters are determined from values in Table 1.

Dimensionless parameter	Relation with dimensional parameters	Typical value
d_{SiO}	$\frac{D_{\mathrm{SiO}}}{D_{\mathrm{O_2}}}$	0.8298
$d_{\mathrm{SiO_2}}$	$\frac{D_{\mathrm{SiO_2}}}{D_{\mathrm{O_2}}}$	0.8298
d_{CO}	$\frac{D_{\mathrm{CO}}}{D_{\mathrm{O_2}}}$	3.829×10^{-2}
$d_{\mathrm{CO_2}}$	$\frac{D_{\mathrm{CO_2}}}{D_{\mathrm{O_2}}}$	3.040×10^{-2}
Le	$\frac{\kappa}{\rho_0 c_p D_{\mathrm{O_2}}}$	0.3470
a	$\frac{C_{\mathrm{SiO},0}}{C_{\mathrm{O_2},0}}$	$10^{-3} - 0.2$
ε	$\frac{A_2}{A_1} \exp\left(\frac{E_1 - E_2}{RT_1}\right)$	6.031×10^{-3}
h_1	$\frac{C_{\mathrm{SiO},0} \Delta H_1}{2(T_1 - T_2)\rho_0 c_p}$	0.8591
h_2	$\frac{C_{\mathrm{CO},0} \Delta H_2}{2(T_1 - T_2)\rho_0 c_p}$	0.3073
α_1	$\exp\left(-\frac{E_1}{R}\left(\frac{1}{T_2} - \frac{1}{T_1}\right)\right)$	0.32
α_2	$\exp\left(-\frac{E_2}{R}\left(\frac{1}{T_2} - \frac{1}{T_1}\right)\right)$	0.659
ζ_1	$\frac{\pi \rho_p J_0 (s_{\min})^3}{4MA_1 C_{\mathrm{O_2},0} C_{\mathrm{SiO_2},0}} \exp\left(\frac{E_1}{RT_1}\right)$	3.875×10^{-2}
ζ_2	$\frac{\pi L_V J_0 (s_{\min})^3}{4\rho_0 c_p A_1 C_{\mathrm{O_2},0}(T_1 - T_2)} \exp\left(\frac{E_1}{RT_1}\right)$	0.1024
d_p	$\frac{D_p}{D_{\mathrm{O_2}}}$	2.128×10^{-6}
T^*	$\frac{T_2}{T_1 - T_2}$	1.677
G^*	$\frac{MC_{\mathrm{SiO_2},0}\sqrt{T_1 - T_2}}{\rho_p A_1 C_{\mathrm{O_2},0} s_{\min}} \sqrt{\frac{k_B}{2\pi m}} \exp\left(\frac{E_1}{RT_1}\right)$	4.39×10^{-2}
J^*	$\frac{J_0 \rho_p}{M \times 10^{23} C_{\mathrm{SiO_2},0}\sqrt{T_1 - T_2}} \sqrt{\frac{\pi m}{2k_B}}$	1.538×10^4
C_{sat}	$\frac{C_e}{C_{\mathrm{SiO_2},0}}$	$0 - 1$
λ	$\frac{16\pi\gamma^3 v_C^2}{3k_B^3 T_2^3}$	0.3474

With these scalings and dropping the over tilde notation, the dimensionless equations read

$$\frac{\partial C_{\mathrm{O_2}}}{\partial t} - \frac{\partial^2 C_{\mathrm{O_2}}}{\partial z^2} = -\frac{a}{2}\left(f_1(T) C_{\mathrm{O_2}} C_{\mathrm{SiO}} + \varepsilon f_2(T) C_{\mathrm{O_2}} C_{\mathrm{CO}}\right), \tag{14a}$$

$$\frac{\partial C_{\mathrm{SiO}}}{\partial t} - d_{\mathrm{SiO}} \frac{\partial^2 C_{\mathrm{SiO}}}{\partial z^2} = -f_1(T) C_{\mathrm{O_2}} C_{\mathrm{SiO}}, \tag{14b}$$

$$\frac{\partial C_{\mathrm{SiO_2}}}{\partial t} - d_{\mathrm{SiO_2}}\frac{\partial^2 C_{\mathrm{SiO_2}}}{\partial z^2} = f_1(T)C_{\mathrm{O_2}}C_{\mathrm{SiO}} - \zeta_1 G(z,t)M_2, \tag{14c}$$

$$\frac{\partial C_{\mathrm{CO}}}{\partial t} - d_{\mathrm{CO}}\frac{\partial^2 C_{\mathrm{CO}}}{\partial z^2} = -\varepsilon f_2(T)C_{\mathrm{O_2}}C_{\mathrm{CO}}, \tag{14d}$$

$$\frac{\partial C_{\mathrm{CO_2}}}{\partial t} - d_{\mathrm{CO_2}}\frac{\partial^2 C_{\mathrm{CO_2}}}{\partial z^2} = \varepsilon f_2(T)C_{\mathrm{O_2}}C_{\mathrm{CO}}, \tag{14e}$$

$$\frac{\partial T}{\partial t} - Le\frac{\partial^2 T}{\partial z^2} = h_1 f_1(T)C_{\mathrm{O_2}}C_{\mathrm{SiO}} + \varepsilon h_2 f_2(T)C_{\mathrm{O_2}}C_{\mathrm{CO}} + \zeta_2 G(z,t)M_2, \tag{14f}$$

$$\frac{\partial M_0}{\partial t} - d_p\frac{\partial^2 M_0}{\partial z^2} = G^* J(z,t), \tag{14g}$$

$$\frac{\partial M_1}{\partial t} - d_p\frac{\partial^2 M_1}{\partial z^2} = G^* J(z,t) + G^* G(z,t)M_0, \tag{14h}$$

$$\frac{\partial M_2}{\partial t} - d_p\frac{\partial^2 M_2}{\partial z^2} = G^* J(z,t) + 2G^* G(z,t)M_1, \tag{14i}$$

for $-\infty < z < \infty$, $t > 0$. The dimensionless Arrhenius terms in the reaction rates have the form

$$f_j(T) = \exp\left(-\frac{E_j}{R}\left(\frac{1}{(T_1 - T_2)T + T_2} - \frac{1}{T_1}\right)\right), \quad j = 1, 2, \tag{15}$$

and the nondimensional particle growth and nucleation rates are given by

$$G = \sqrt{T + T^*}\,(C_{\mathrm{SiO_2}} - C_{\mathrm{sat}})\,\mathcal{H}\,(C_{\mathrm{SiO_2}} - C_{\mathrm{sat}}) \quad \text{and} \tag{16}$$

$$J = \exp\left(-\frac{\lambda}{\left(\frac{T}{T^*} + 1\right)^3 \ln^2\left(\frac{C_{\mathrm{SiO_2}}}{C_{\mathrm{sat}}}\right)}\right),$$

respectively. The dimensionless initial conditions are the following:

$$C_X = \frac{C_{X,\mathrm{initial}}(z)}{C_{X,0}}, \quad T = \frac{T_{\mathrm{initial}}(z) - T_2}{T_1 - T_2}, \quad M_0 = M_1 = M_2 = 0 \quad \text{at} \quad t = 0. \tag{17}$$

In the nondimensionalization we assumed that the input value of all the chemical species is the same except for the oxygen, that is, $C_{\mathrm{SiO},0} = C_{\mathrm{SiO_2},0} = C_{\mathrm{CO},0} = C_{\mathrm{CO_2},0}$. Thus, a represents the ratio of the maximum concentration of these species to the maximum concentration of oxygen, ε is the ratio between the reaction rates, and h_1 and h_2 measure the balance between the reactant concentration needed to give off heat and the role of the respective reaction on generating heat.

Finally, the particle formation and growth problem in nondimensional form reads

$$\frac{\partial n}{\partial t} - d_p\frac{\partial^2 n}{\partial z^2} = -G^* G(z,t)\frac{\partial n}{\partial s} \quad \text{for} \quad -\infty < z < \infty, \quad s > 1, \quad t > 0, \tag{18a}$$

$$n = 0 \quad \text{at} \quad t = 0, \quad \text{and} \quad Gn = J \quad \text{at} \quad s = 1. \tag{18b}$$

3. The case of well-mixed chemical species. We first consider the case where the chemical species are well-mixed, with uniform initial concentrations and temperature for all $z \in \mathbb{R}$, so that the concentrations and temperature are independent

of z for all $t \geq 0$. This limit is best viewed as a simplification of the spatial structure taken in order to better qualitatively understand the dynamics taking place within the interior of the reaction zone, whereas in the next section we will more accurately depict the macroscopic scale structure of the reaction zone between two larger non-reacting regions. Under this assumption, (14a)–(14i) reduce to the system

$$\frac{\mathrm{d}C_{\mathrm{O}_2}}{\mathrm{d}t} = -\frac{a}{2}\left(f_1(T)C_{\mathrm{O}_2}C_{\mathrm{SiO}} + \varepsilon f_2(T)C_{\mathrm{O}_2}C_{\mathrm{CO}}\right), \tag{19a}$$

$$\frac{\mathrm{d}C_{\mathrm{SiO}}}{\mathrm{d}t} = -f_1(T)C_{\mathrm{O}_2}C_{\mathrm{SiO}}, \tag{19b}$$

$$\frac{\mathrm{d}C_{\mathrm{SiO}_2}}{\mathrm{d}t} = f_1(T)C_{\mathrm{O}_2}C_{\mathrm{SiO}} - \zeta_1 G(t)M_2, \tag{19c}$$

$$\frac{\mathrm{d}C_{\mathrm{CO}}}{\mathrm{d}t} = -\varepsilon f_2(T)C_{\mathrm{O}_2}C_{\mathrm{CO}}, \tag{19d}$$

$$\frac{\mathrm{d}C_{\mathrm{CO}_2}}{\mathrm{d}t} = \varepsilon f_2(T)C_{\mathrm{O}_2}C_{\mathrm{CO}}, \tag{19e}$$

$$\frac{\mathrm{d}T}{\mathrm{d}t} = h_1 f_1(T)C_{\mathrm{O}_2}C_{\mathrm{SiO}} + \varepsilon h_2 f_2(T)C_{\mathrm{O}_2}C_{\mathrm{CO}} + \zeta_2 G(t)M_2, \tag{19f}$$

$$\frac{\mathrm{d}M_0}{\mathrm{d}t} = G^* J(t), \tag{19g}$$

$$\frac{\mathrm{d}M_1}{\mathrm{d}t} = G^* J(t) + G^* G(t)M_0, \tag{19h}$$

$$\frac{\mathrm{d}M_2}{\mathrm{d}t} = G^* J(t) + 2G^* G(t)M_1, \tag{19i}$$

for $t > 0$, while the initial conditions become

$$C_{\mathrm{O}_2} = C_{\mathrm{SiO}} = C_{\mathrm{CO}} = T = 1, \quad C_{\mathrm{SiO}_2} = C_{\mathrm{CO}_2} = M_0 = M_1 = M_2 = 0 \quad \text{at} \quad t = 0. \tag{20}$$

The particle formation and growth system (18) reduces to

$$\frac{\partial n}{\partial t} = -G^* G(t)\frac{\partial n}{\partial s} \quad \text{for} \quad s > 1, \quad t > 0, \tag{21a}$$

$$n = 0 \quad \text{at} \quad t = 0, \quad \text{and} \quad Gn = J \quad \text{at} \quad s = 1. \tag{21b}$$

3.1. Analytical solution to the chemical-temperature problem. For analytical tractability we shall set $\zeta_1 = \zeta_2 = 0$. Several conservation laws for the concentrations and temperature are apparent and we no longer need to solve for the moments of the distribution since they decouple from the system. Combining (19d) and (19e), and (19b) and (19c), we obtain

$$C_{\mathrm{CO}_2} = 1 - C_{\mathrm{CO}}, \quad C_{\mathrm{SiO}_2} = 1 - C_{\mathrm{SiO}}, \tag{22a}$$

respectively. Now using (19a), (19b), and (19d), we find

$$C_{\mathrm{O}_2} = 1 - \frac{a}{2}[(1 - C_{\mathrm{SiO}}) + (1 - C_{\mathrm{CO}})], \tag{22b}$$

and finally combining (19b), (19d), and (19f), we obtain

$$T = 1 + h_1(1 - C_{\mathrm{SiO}}) + h_2(1 - C_{\mathrm{CO}}). \tag{22c}$$

Making use of these conservation laws, we eliminate C_{O_2}, C_{SiO_2}, C_{CO_2}, and T, obtaining the system

$$\frac{\mathrm{d}C_{\mathrm{SiO}}}{\mathrm{d}t} = -f_1\left(1+h_1(1-C_{\mathrm{SiO}})+h_2(1-C_{\mathrm{CO}})\right) \times \left(1-\frac{a}{2}[(1-C_{\mathrm{SiO}})+(1-C_{\mathrm{CO}})]\right) C_{\mathrm{SiO}}, \tag{23a}$$

$$\frac{\mathrm{d}C_{\mathrm{CO}}}{\mathrm{d}t} = -\varepsilon f_2\left(1+h_1(1-C_{\mathrm{SiO}})+h_2(1-C_{\mathrm{CO}})\right) \times \left(1-\frac{a}{2}[(1-C_{\mathrm{SiO}})+(1-C_{\mathrm{CO}})]\right) C_{\mathrm{CO}}, \tag{23b}$$

subject to $C_{\mathrm{SiO}}(0) = C_{\mathrm{CO}}(0) = 1$.

3.1.1. Multiple timescale analysis. In order to understand the dynamics from (23), we first make several observations. First, for any $C_{\mathrm{SiO}}(t), C_{\mathrm{CO}}(t) \in (0,1]$, we have that

(24a)
$$0 < f_1\left(1+h_1(1-C_{\mathrm{SiO}})+h_2(1-C_{\mathrm{CO}})\right)\left(1-\frac{a}{2}[(1-C_{\mathrm{SiO}})+(1-C_{\mathrm{CO}})]\right) C_{\mathrm{SiO}} \leq f_1\left(1+h_1+h_2\right),$$

(24b)
$$0 < f_2\left(1+h_1(1-C_{\mathrm{SiO}})+h_2(1-C_{\mathrm{CO}})\right)\left(1-\frac{a}{2}[(1-C_{\mathrm{SiO}})+(1-C_{\mathrm{CO}})]\right) C_{\mathrm{CO}} \leq f_2\left(1+h_1+h_2\right),$$

thus $C_{\mathrm{SiO}}(t)$ and $C_{\mathrm{CO}}(t)$ are monotone decreasing from 1 to 0. Second, since $0 < \varepsilon \ll 1$, the dynamics of (23b) are on a slower timescale than those of (23a). Introducing the slow timescale $\tau = \varepsilon t$, and writing $C_{\mathrm{CO}} = C_{\mathrm{CO}}(\tau)$, we have

$$\frac{\mathrm{d}C_{\mathrm{SiO}}}{\mathrm{d}t} = -f_1\left(1+h_1(1-C_{\mathrm{SiO}}(t))+h_2(1-C_{\mathrm{CO}}(\varepsilon t))\right) \times \left(1-\frac{a}{2}[(1-C_{\mathrm{SiO}}(t))+(1-C_{\mathrm{CO}}(\varepsilon t))]\right) C_{\mathrm{SiO}}(t), \tag{25a}$$

$$\frac{\mathrm{d}C_{\mathrm{CO}}}{\mathrm{d}\tau} = -f_2\left(1+h_1(1-C_{\mathrm{SiO}}(\tau/\varepsilon))+h_2(1-C_{\mathrm{CO}}(\tau))\right) \times \left(1-\frac{a}{2}[(1-C_{\mathrm{SiO}}(\tau/\varepsilon))+(1-C_{\mathrm{CO}}(\tau))]\right) C_{\mathrm{CO}}(\tau). \tag{25b}$$

In (25a), $C_{\mathrm{CO}}(\varepsilon t)$ is slowly varying and can be treated as a constant at lowest order, relative to the timescale on which $C_{\mathrm{SiO}}(t)$ varies. Similarly, in (25b), $C_{\mathrm{SiO}}(\tau/\varepsilon)$ is rapidly varying and nears its equilibrium value before $C_{\mathrm{CO}}(\tau)$ responds. Therefore, we approximate (25) by approximating $C_{\mathrm{CO}}(\varepsilon t) = 1$ on the timescale t and $C_{\mathrm{SiO}}(\tau/\varepsilon) = 0$ on the timescale τ. We obtain

$$\frac{\mathrm{d}C_{\mathrm{SiO}}}{\mathrm{d}t} = -f_1\left(1+h_1(1-C_{\mathrm{SiO}}(t))\right)\left(1-\frac{a}{2}(1-C_{\mathrm{SiO}}(t))\right) C_{\mathrm{SiO}}(t), \tag{26a}$$

$$\frac{\mathrm{d}C_{\mathrm{CO}}}{\mathrm{d}\tau} = -f_2\left(1+h_1+h_2(1-C_{\mathrm{CO}}(\tau))\right)\left(1-\frac{a}{2}[1+(1-C_{\mathrm{CO}}(\tau))]\right) C_{\mathrm{CO}}(\tau). \tag{26b}$$

Solving (26) by quadrature, we obtain the implicit relations

$$\int_{C_{\mathrm{SiO}}}^{1} \frac{\mathrm{d}\xi}{f_1\left(1+h_1(1-\xi)\right)\left(1-\frac{a}{2}(1-\xi)\right)\xi} = t, \qquad \int_{C_{\mathrm{CO}}}^{1} \frac{\mathrm{d}\xi}{f_2\left(1+h_1+h_2(1-\xi)\right)\left(1-\frac{a}{2}(2-\xi)\right)\xi} = \tau, \tag{27}$$

where it is clear that $C_{\mathrm{SiO}}, C_{\mathrm{CO}} \to 0$ as $t \to \infty$, as expected. In order to obtain more explicit representations of the solutions, we make further assumptions.

3.1.2. Approximating the Arrhenius terms. We shall at times find it convenient to approximate the Arrhenius terms in the reaction kinetics (15) with linear approximations, $f_j(T) \approx F_j(T)$, where

$$F_j(T) = \alpha_j + (1-\alpha_j)T \quad \text{with} \quad \alpha_j = \exp\left(-\frac{E_j}{R}\left(\frac{1}{T_2}-\frac{1}{T_1}\right)\right). \tag{28}$$

The error estimate of this approximation based on the initial data for T is $\max_{T\in[0,1]} \frac{|f_1(T)-F_1(T)|}{f_1(T)} = 0.031$ and $\max_{T\in[0,1]} \frac{|f_2(T)-F_2(T)|}{f_2(T)} = 0.027$ for parameter values in Table 2. Hence, the maximal relative error for $0 \le T \le 1$ is around 3%. Later on we will see that at certain spatial locations and times the temperature can go up to 2 approximately. In this case, the maximal relative error for $0 \le T \le 2$ is around 5% for F_1 and 8% for F_2. We conclude that the error of this approximation is low enough over the range of temperatures considered so that the qualitative behavior of the solutions is unaltered. Notice that the temperature will only go beyond 2 when we solve the full problem numerically; however, there is no need for an approximation of the Arrhenius terms in this case.

3.1.3. Small a asymptotics. Making use of the approximation (28), we write

$$\frac{\mathrm{d}C_{\mathrm{SiO}}}{\mathrm{d}t} = -\left(\alpha_1 + (1-\alpha_1)[1+h_1(1-C_{\mathrm{SiO}})]\right)\left(1-\frac{a}{2}(1-C_{\mathrm{SiO}})\right)C_{\mathrm{SiO}}, \tag{29a}$$

$$\frac{\mathrm{d}C_{\mathrm{CO}}}{\mathrm{d}\tau} = -\left(\alpha_2 + (1-\alpha_2)[1+h_1+h_2(1-C_{\mathrm{CO}})]\right)\left(1-\frac{a}{2}[1+(1-C_{\mathrm{CO}})]\right)C_{\mathrm{CO}}. \tag{29b}$$

Recall that $0 < a \le 0.2$. We therefore treat a as a small parameter, $a \ll 1$, and at lowest order in a, the ODEs (29) become quadratic rather than cubic. Solving these lowest order equations subject to $C_{\mathrm{SiO}}(0) = 1$ and $C_{\mathrm{CO}}(0) = 1$, respectively, we find that the asymptotic solutions in the small a limit are

$$C_{\mathrm{SiO}}(t) = \frac{1+h_1\,(1-\alpha_1)}{\exp\left(\left[1+h_1\,(1-\alpha_1)\right]t\right)+h_1\,(1-\alpha_1)} + \mathcal{O}(a), \tag{30a}$$

$$C_{\mathrm{CO}}(t) = \frac{1+(h_1+h_2)\,(1-\alpha_2)}{(1+h_1\,(1-\alpha_2))\exp\left(\left[1+(h_1+h_2)\,(1-\alpha_2)\right]\varepsilon t\right)+h_2\,(1-\alpha_2)} + \mathcal{O}(a). \tag{30b}$$

Asymptotic solutions for all remaining quantities can be obtained from (30) and the earlier mentioned conservation laws (22a)–(22c). We plot the approximate solutions in Figure 3 for one small value of a (left) and the upper bound $a = 0.2$ (right). We see that since C_{CO} and C_{CO_2} evolve on a slower timescale than the rest of the chemical concentrations, the second reaction has not happened yet, while the first one finishes within the selected timescale. When comparing the analytical approximations (solid line) to the numerical simulations (dashed line) we find good agreement, even for relatively large values of a, so the analytical solution retains validity in the physically relevant parameter regime.

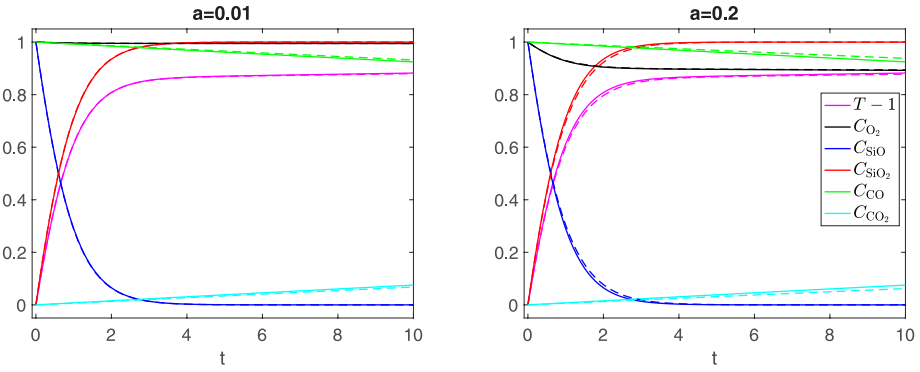

FIG. 3. *Dimensionless chemical concentrations and temperature as indicated in the legend from solving the problem* (19)–(20) *numerically (dashed line) and analytically (solid line) assuming* $\zeta_1 = \zeta_2 = 0$. *We compare the solutions for* $a = 0.01$ *(left) and* $a = 0.2$ *(right). We fix* $C_{sat} = 0.1$, *with other parameters taking values listed in Table* 2.

3.2. Analytical solution of the particle density equation. We find an analytical solution for the particle density function by solving the problem (21) in terms of the growth rate G and nucleation rate J as given in (16), which depend on $C_{\mathrm{SiO_2}}$ and T. First, we define $t_{\min}$ to be the minimal value of t such that $C_{\mathrm{SiO_2}}(t_{\min}) = C_{\mathrm{sat}}$. Noting that $1 - C_{\mathrm{SiO}}(t_{\min}) = C_{\mathrm{SiO_2}}(t_{\min}) = C_{\mathrm{sat}}$, and employing the asymptotic solution (30a), we find

$$t_{\min} = \frac{1}{1 + h_1\,(1-\alpha_1)}\log\left(\frac{1 + h_1\,(1-\alpha_1)\,C_{\mathrm{sat}}}{1 - C_{\mathrm{sat}}}\right) + \mathcal{O}(a) \tag{31}$$

as $a \to 0$. In the case where $t \le t_{\min}$, (21a) reduces to $\partial n/\partial s = 0$ for $s > 1$, with $n = 0$ at $t = 0$, hence the solution is $n = 0$. This makes sense since no particles are formed before the concentration reaches saturation. For the second case where $t > t_{\min}$, we use the method of characteristics to obtain a parametric solution for n. For characteristics emanating from $t = t_{\min}$, given by

$$s = s_1 + G^* \int_{t_{\min}}^{t} G(\tau)\mathrm{d}\tau \tag{32}$$

with $s_1 > 1$, the solution is always $n = 0$. For characteristic curves emerging from $s = 1$, given implicitly by

$$s = 1 + G^* \int_{t_1}^{t} G(\tau)\mathrm{d}\tau \tag{33}$$

with $t_1 > t_{\min}$, the solution is

$$n = \frac{J(t_1)}{G(t_1)}. \tag{34}$$

In Figure 4(a), we plot the characteristic curves, with the red curve corresponding to the dividing characteristic that bounds both regions and is given implicitly by

$$s^*(t) = 1 + G^* \int_{t_{\min}}^{t} G(\tau)\mathrm{d}\tau. \tag{35}$$

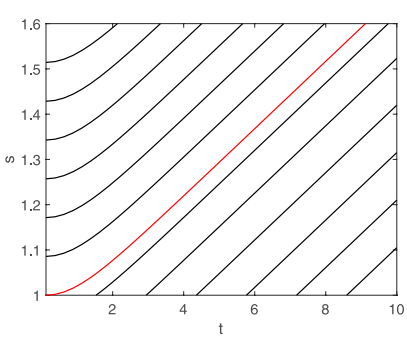

(a) Characteristic curves

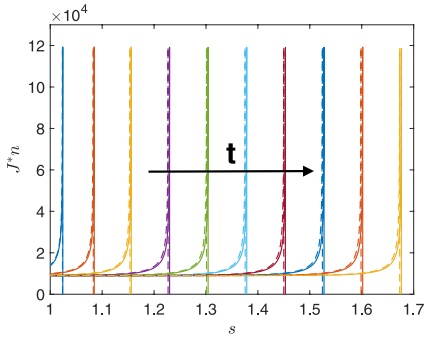

(b) Number density functions

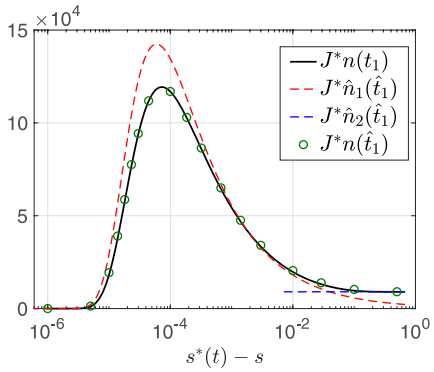

(c) Semi-log plot for the number density function (black) and asymptotic approximations (dashed lines and circles).

FIG. 4. (a) *Characteristic curves corresponding to problem* (21) *where the red line is the limiting curve given by* (35). *In* (b) *we show the dimensionless number density function of particles for different values of* t *from* 1 *to* 10 *with an increment of* 1. *The curves are obtained from solving the problem* (19a)–(19f), *with* $\zeta_1, \zeta_2 = 0$, *numerically (dashed line) and analytically (solid line) for* $a = 0.2$ *and using the formulae* (33) *and* (34) *for* n. *In* (c) *we provide a semi-log plot for the number density functions from* (b) *(black solid line), for* n *with asymptotic approximations for the characteristics* (40) *(green circles), and for the asymptotic approximations of the peak* (41) *(red dashed line) and uniform* (44) *(blue dashed line) parts of the distribution. The legend indicates the meaning of each curve. We have chosen* $C_{sat} = 0.1$ *and have scaled* n *with the dimensionless parameter* $J^* = J_0/(10^{23}G_0)$ *from Table* 2.

In the region above this curve the solution is $n = 0$, whereas below it is given by (34). In Figure 4(b), we show the solution for n given by (33) and (34), where we take C_{SiO_2} and T from both the analytical approximations and numerical simulations in the previous section with $a = 0.2$. The main difference we see between the particle density functions obtained using both approximations is the position of the peaks. This is due to the small shift in the C_{SiO_2} curves in Figure 3; the concentration will reach the saturation point at a slightly different time $t_{\min}$. Here, we have chosen $C_{\mathrm{sat}} = 0.1$, thus $t_{\min} = 0.106$ in the numerics (dashed line) and $t_{\min} = 0.103$ in the analytics (solid line). Since in the latter case the particles start growing at an earlier time, they grow to be larger.

In Figure 4(b), we see that as time evolves the peaks move to the right, meaning that the particles grow. With respect to the shape of n for a specific time, we find

a uniform distribution at smaller sizes and a peak around the largest sizes. The largest number of particles are of the largest sizes, and these particles originated very close to $t = t_{\min}$, with their change in diameter over time (the position of the peaks) determined approximately by the characteristic $s^*(t)$ highlighted in red in Figure 4(a). We show the solution corresponding to the last peak in Figure 4(b) ($t = 10$) in a semi-log plot in Figure 4(c) with a black solid curve.

In order to better understand the parameter dependence of the peak, we consider an asymptotic analysis near the red characteristic. We use the approximated solutions for C_{SiO_2} and T from section 3.1, neglecting terms which evolve on the slow timescale $\tau = \epsilon t$ and setting $C_{\mathrm{CO}}(t) \approx 1$ for $t \ll \varepsilon^{-1}$. We also neglect $\mathcal{O}(a)$ terms. From Figure 4(c) (black solid line), there are two timescales to consider. The first timescale corresponds to $0 < t - t_{\min} \ll 1$, for which $0 < s^*(t) - s \ll 1$, and we have the observed peak in Figures 4(b) and 4(c). For $t - t_{\min} \gg 1$, we have the flat region of uniform distribution away from the peak, which corresponds to $C_{\mathrm{SiO}_2} \sim 1$ and $T(t) \sim 1 + h_1$, as seen in Figure 3. The reaction leading to particle growth happens before the very large timescales on which C_{CO} will play a role, so we consider $1 \ll t - t_{\min} \ll \varepsilon^{-1}$ for our second timescale.

3.2.1. The small timescale, $0 < t - t_{\min} \ll 1$. Expanding the analytical solutions for C_{SiO_2} and T, (22a) and (22c) with (30), found in section 3.1 in $t - t_{\min}$, we write

(36a)
$$C_{\mathrm{SiO}_2}(t) = C_{\mathrm{sat}} + (1 - C_{\mathrm{sat}})\,(1 + h_1(1 - \alpha_1)C_{\mathrm{sat}})\,(t - t_{\min}) + \mathcal{O}\left((t - t_{\min})^2\right),$$

(36b)
$$T(t) = 1 + h_1 C_{\mathrm{sat}} + h_1(1 - C_{\mathrm{sat}})\,(1 + h_1(1 - \alpha_1)C_{\mathrm{sat}})\,(t - t_{\min}) + \mathcal{O}\left((t - t_{\min})^2\right).$$

These approximations allow us to approximate the characteristic curves (33) by the formula

(37)
$$s = 1 + \frac{G^*}{2}\sqrt{T^* + 1 + h_1 C_{\mathrm{sat}}}(1 - C_{\mathrm{sat}})\,(1 + h_1(1 - \alpha_1)C_{\mathrm{sat}})\left\{(t - t_{\min})^2 - (t_1 - t_{\min})^2\right\},$$

where we have used

$$\sqrt{T^* + 1 + h_1 C_{\mathrm{sat}} + h_1(1 - C_{\mathrm{sat}})\,(1 + h_1(1 - \alpha_1)C_{\mathrm{sat}})\,(t - t_{\min})} \approx \sqrt{T^* + 1 + h_1 C_{\mathrm{sat}}}.$$

We find

(38)
$$t_1 = t_{\min} + \sqrt{(t - t_{\min})^2 - \frac{s - 1}{\frac{G^*}{2}\sqrt{T^* + 1 + h_1 C_{\mathrm{sat}}}(1 - C_{\mathrm{sat}})\,(1 + h_1(1 - \alpha_1)C_{\mathrm{sat}})}},$$

and similarly for (35), we obtain

$$s^*(t) = 1 + \frac{G^*}{2}\sqrt{T^* + 1 + h_1 C_{\mathrm{sat}}}(1 - C_{\mathrm{sat}})\,(1 + h_1(1 - \alpha_1)C_{\mathrm{sat}})\,(t - t_{\min})^2. \tag{39}$$

Therefore, we may write

$$t_1 \approx \hat{t}_1 = t_{\min} + \sqrt{\frac{s^*(t) - s}{\frac{G^*}{2}\sqrt{T^* + 1 + h_1 C_{\mathrm{sat}}}(1 - C_{\mathrm{sat}})\,(1 + h_1(1 - \alpha_1)C_{\mathrm{sat}})}}, \tag{40}$$

where it will be convenient to define the moving coordinate $S = s^*(t) - s$. We remark that the small $t - t_{\min}$ regime corresponds to the small S regime. We evaluate the exact solution $n(t_1)$ at the explicit approximation of t_1 as given by (40) and plot it in Figure 4(c) with green circles to find that it matches the real solution (black solid line) everywhere. As such, the approximate characteristic curves result in nearly the same exact solution (plotted numerically) and do not introduce significant error.

From the implicit form of the exact solution, $n(s,t) = J(t_1)/G(t_1)$, we now use the approximation of t_1 to construct an approximation $\hat{n}_1$ to n which is explicit in the variables. We find

$$n = \frac{\exp\left\{-\lambda\left(\frac{T(t_1)}{T^*}+1\right)^{-3}\left[\ln\left(\frac{C_{\mathrm{SiO_2}}(t_1)}{C_{\mathrm{sat}}}\right)\right]^{-2}\right\}}{\sqrt{T^*+T(t_1)}\,(C_{\mathrm{SiO_2}}(t_1)-C_{\mathrm{sat}})} \approx \hat{n}_1(S) = \frac{\Gamma}{\sqrt{S}}\exp\left(-\frac{\Lambda}{S}\right), \tag{41a}$$

where

$$\Gamma = \sqrt{\frac{G^*}{2\sqrt{T^*+1+h_1C_{\mathrm{sat}}}(1-C_{\mathrm{sat}})\,(1+h_1(1-\alpha_1)C_{\mathrm{sat}})}}, \tag{41b}$$

$$\Lambda = \frac{\lambda G^* {T^*}^3 C_{\mathrm{sat}}^2}{2\,(T^*+1+h_1C_{\mathrm{sat}})^{5/2}\,(1-C_{\mathrm{sat}})\,(1+h_1(1-\alpha_1)C_{\mathrm{sat}})}. \tag{41c}$$

Here Γ and Λ are constants which depend on model parameters. From (41a), the position and height of the peak are given by $s_{\mathrm{p}}{=}s^*(t){-}2\Lambda$ and $\hat{n}_1(s_{\mathrm{p}}){=}\Gamma\exp(-1/2)/\sqrt{2\Lambda}$, respectively. Note that the position is time-dependent. Using Table 2 and $C_{\mathrm{sat}} = 0.1$, we find $\Gamma = 0.117$ and $\Lambda = 3.268\times10^{-5}$. We plot the approximation (41a) with a red dashed curve in Figure 4(c) and find that the width of the peak is well represented, as is the rate of change on each side of the peak, while the height of the peak is slightly overestimated (and would, in principle, be improved by the inclusion of higher order terms).

3.2.2. The larger timescale, $1 \ll t - t_{\min} \ll \varepsilon^{-1}$. On the timescale $1 \ll t - t_{\min} \ll \varepsilon^{-1}$, we have $C_{\mathrm{SiO_2}}(t) = 1 - \mathcal{O}(\exp\{-(1+h_1(1-\alpha_1))t\})$ and $T(t) = 1 + h_1 - \mathcal{O}(\exp\{-(1+h_1(1-\alpha_1))t\})$, and we approximate $C_{\mathrm{SiO_2}}(t) \approx 1$ and $T(t) \approx 1+h_1$. Similar to the above, we find

$$\begin{aligned} s &= 1 + G^*\int_{t_1}^{t}\sqrt{T^*+T(\tau)}\,(C_{\mathrm{SiO_2}}(t)-C_{\mathrm{sat}})\,d\tau \\ &= 1 + G^*\sqrt{T^*+1+h_1}(1-C_{\mathrm{sat}})\,(t-t_1)\,, \end{aligned} \tag{42}$$

$$s^*(t) = 1 + G^*\sqrt{T^*+1+h_1}(1-C_{\mathrm{sat}})\,(t-t_{\min})\,. \tag{43}$$

From this we note that the characteristic curves become lines once $S = \mathcal{O}(1)$, consistent with what is observed in Figure 4(a) once s is an $\mathcal{O}(1)$ distance away from the curve $s^*(t)$ (shown in red). Manipulating these equations, we obtain

$$\begin{aligned} t_1 &= t_{\min} + \frac{S}{G^*\sqrt{T^*+1+h_1}(1-C_{\mathrm{sat}})} \quad \text{and} \\ n \approx \hat{n}_2 &= \frac{\exp\left\{-\lambda\left(\frac{1+h_1}{T^*}+1\right)^{-3}\left[\ln\left(\frac{1}{C_{\mathrm{sat}}}\right)\right]^{-2}\right\}}{\sqrt{T^*+1+h_1}\,(1-C_{\mathrm{sat}})}, \end{aligned} \tag{44}$$

where $\hat{n}_2$ is a constant and $S = s^*(t) - s$ is the moving coordinate. Using parameter values from Table 2 as well as $C_{\text{sat}} = 0.1$, we find $\hat{n}_2 \approx 5.773 \times 10^{-1}$, and scaling with J^* we have $\hat{n}_2 \approx 5.773 \times 10^{-1} J^* = 8.879 \times 10^3$, which is consistent with the value n levels off to in Figure 4(c) as S becomes $\mathcal{O}(1)$ ($n \approx \hat{n}_2$ corresponds to the blue dashed line).

To summarize, the asymptotic solutions provide an explicit formula for n in terms of well-known parameters, capturing the qualitative behavior of the particle size distribution, with the small time ($0 < t - t_{\min} \ll 1$) approximation $\hat{n}_1(\hat{t}_1)$ capturing the peak and the intermediate time ($1 \ll t - t_{\min} \ll \varepsilon^{-1}$) approximation $\hat{n}_2(\hat{t}_1)$ providing the uniform distribution away from the peak. The largest timescale, $t - t_{\min} \gg \varepsilon^{-1}$, will not play a strong role in modifying the distribution n (which is on the two timescales felt by C_{SiO_2}), and hence we do not consider it.

3.3. Numerical solution of the fully coupled system for $\zeta_1, \zeta_2 > 0$. We solve the full problem (19) with $\zeta_1, \zeta_2 > 0$ numerically and then use the analytical solution obtained for n in section 3.2, providing simulations in Figure 5. The SiO_2 concentration (red curve in Figure 5(a)) reaches a maximum while the SiO combustion reaction occurs, and it later decreases as SiO_2 is consumed due to particle growth. The temperature, shown in Figure 5(b), also increases initially due to the combustion reaction, yet further increases due to energy given off during particle formation. The peak in the particle density function, n, plotted in Figure 5(d), moves to the right with time as particles grow. However, as the available C_{SiO_2} decreases toward the saturation concentration (around $t = 25$), the value of $n = J/G$ at $s = 1$ gets very large forming a second peak around the smallest particle size. Many particles are created (due to the increasing temperature), but they cannot grow large (due to the limited availability of SiO_2). In Figure 5(c) we see that particle growth stops after some critical time, and the maximum particle size is given by the value that the red characteristic converges to, approximately 2.2 for the case plotted. In Figure 5(e) we plot the first few moments of the distribution n, the number of particles, M_0, the mean, $\mu = M_1/M_0$, and the variance, $\sigma^2 = M_2/M_0 - \mu^2$. All moments tend to a constant for $t > 35$, meaning that the particle density function converges to the red curve in Figure 5(f) as $C_{\text{SiO}_2} \to C_{\text{sat}} = 0.1$. This curve corresponds to a bimodal distribution around the minimum and maximum particle size.

The existence of such a bimodal distribution for particle size is in agreement with previous experimental studies [10] where the particle size distribution of well-dispersed microsilica was found to be bimodal, with a submicron range of particle sizes containing most of the particle mass, and a micron range with fewer but much larger particles. In order to illustrate this finding, in Figure 6 we show a SEM picture of a microsilica sample where we can see few large particles with many small particles attached to them. As the value of C_{sat} increases the distribution turns almost uniform, since less particles are formed and their sizes are smaller since the time interval on which the concentration of SiO_2 is above saturation is reduced.

In Figure 7 we show both peaks on a semi-log plot. Notice that the order of the peaks in Figure 7 is the opposite of the one found in Figure 5(d) and that the values on the horizontal axis of Figure 7(b) are inverted. We use the same approximations as in sections 3.2.1–3.2.2 to obtain an approximation for the large particle-size peak (red dashed line) and uniform distribution between peaks (blue dashed line). However, in the coupled case these approximations are only valid for early times, and the late time peak shown in Figure 7(b) (around $s = 1$) is found numerically.

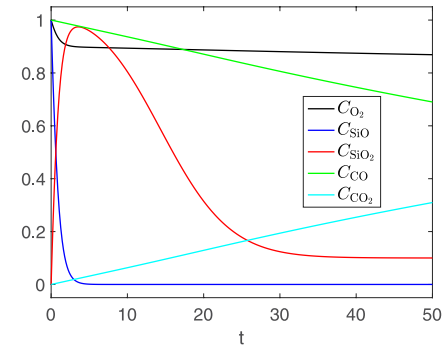

(a) Chemical concentrations

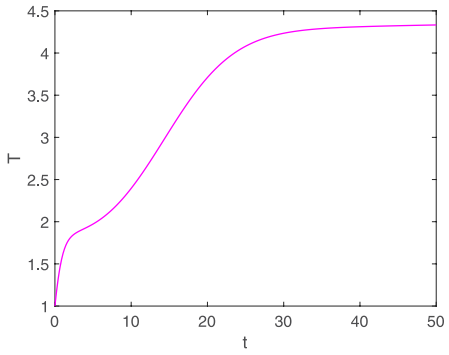

(b) Temperature

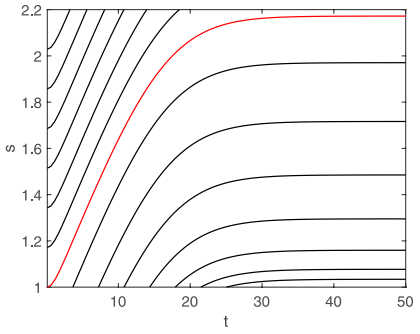

(c) Characteristic curves

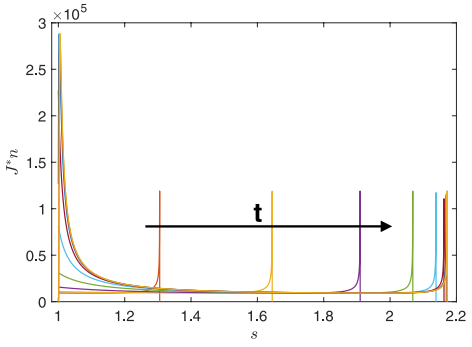

(d) Number density functions

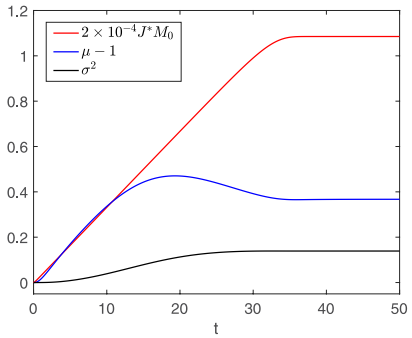

(e) Moments of the distributions for $C_{\text{sat}} = 0.1$

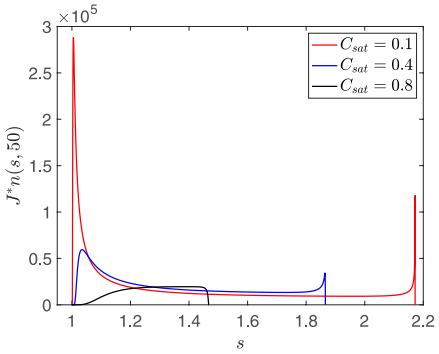

(f) Final particle density function for different C_{sat}

FIG. 5. *Plot of the chemical concentrations* (a), *temperature* (b), *characteristic curves* (c), *number density functions* (d), *and properties of the density distribution* (e) *obtained from solving the fully coupled* ($\zeta_1, \zeta_2 > 0$) *problem* (19) *numerically and using these results in* (33) *and* (34). *We take* $C_{sat} = 0.1$ *and* $a = 0.2$, *with other parameters chosen from Table* 2, *and scale* n *with* J^*. *The direction of the arrow in* (d) *indicates increasing time from* $t_{min} = 0.106$ *to* $t_{min} + 45$, *with an increment of* 5 *at every iteration. As* C_{sat} *is increased* (f), *particle formation initializes later, thus particles have less time to grow, and hence the distribution skews toward smaller sized particles at the final time* $t = 50$. *In* (a) *and* (e), *the legend indicates the meaning of each curve.*

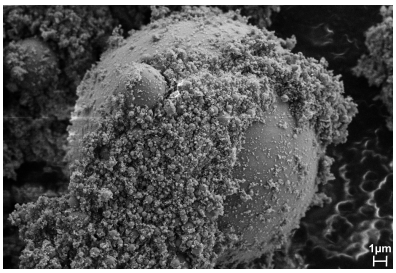

FIG. 6. *SEM image of microsilica particles showing some large particles with many small particles attached to them. Image from Næss* [25].

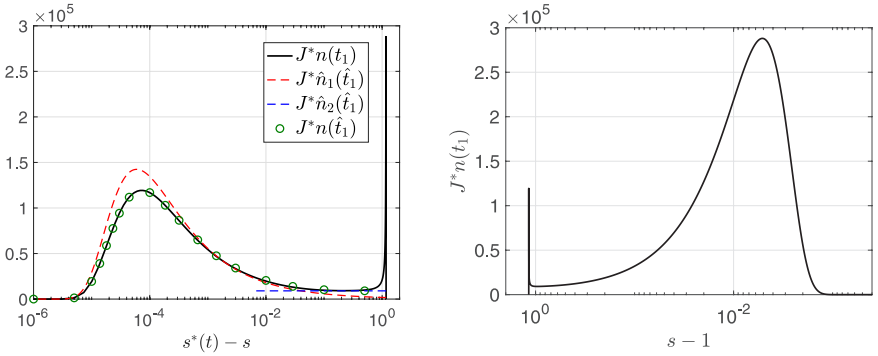

(a) Semi-log plot for n around s^* (b) Semi-log plot for n around 1

FIG. 7. *Semi-log plots for the number density function around* (a) $s = s^*$ *zooming in the large particle-size peak, and around* (b) $s = 1$ *zooming in the small particle-size peak. In* (a) *we show the numerical results for* n *(black solid line), the real solution for* n *with asymptotic approximations for the characteristics as in the uncoupled case (green circles), and the asymptotic approximations for the peak (red dashed line) and uniform part (blue dashed line) taken from* (41a) *and* (44) *respectively, whereas in* (b) *we only show the numerical result. In* (a) *the legend indicates the meaning of each curve.*

4. The case of initially spatially separated chemical species. In this section, we turn our attention to the configuration where chemical concentrations C_{O_2}, C_{SiO}, C_{CO} and temperature are initially spatially heterogeneous, with C_{O_2} present primarily in the region $z > 0$ and C_{SiO} and C_{CO} in the region $z < 0$, with a small overlap. Hence, the dimensionless initial conditions for the concentrations and temperature are such that they are compatible with the following far-field behavior:

$$\text{(45a)} \qquad C_{O_2} = C_{SiO_2} = C_{CO_2} = 0, \quad C_{SiO} = C_{CO} = T = 1 \qquad \text{as} \quad z \to -\infty,$$

$$\text{(45b)} \qquad C_{O_2} = 1, \quad C_{SiO} = C_{CO} = T = 0, \quad \frac{\partial C_{SiO_2}}{\partial z} = \frac{\partial C_{CO_2}}{\partial z} = 0 \quad \text{as} \quad z \to \infty.$$

This is analogous to adding large quantities of oxygen into the top or side of a furnace in more complicated geometries. For large enough temperatures to permit reactions, this configuration results in a narrow reaction layer which then evolves over time. The initial conditions for n and its moments remain unchanged.

4.1. Analytical solution for the coupled chemical-temperature subsystem. The set of equations (14) constitutes a nonlinear, nonlocal reaction-diffusion system. To make any progress outside of numerical simulations, we shall need to make further simplifying assumptions. First, we neglect the coupling to the moments and set ζ_1 and ζ_2 to be equal to zero as in section 3.1. We will include these coupling parameters later when obtaining numerical simulations and compare them to the asymptotic solutions. Further, since $\varepsilon < \zeta_1$ by an order of magnitude, we set $\varepsilon = 0$ and neglect the slower reaction. Finally, observing that $d_{\mathrm{SiO}}, \mathrm{Le} = \mathcal{O}(1)$, we set $d_{\mathrm{SiO}} = \mathrm{Le} = 1$ in order to have equal diffusion rates, which greatly simplifies the derivations. Under these assumptions, the equations governing the dominant reaction are

$$\frac{\partial C_{\mathrm{O}_2}}{\partial t} - \frac{\partial^2 C_{\mathrm{O}_2}}{\partial z^2} = -\frac{a}{2} f_1(T) C_{\mathrm{O}_2} C_{\mathrm{SiO}}, \tag{46a}$$

$$\frac{\partial C_{\mathrm{SiO}}}{\partial t} - \frac{\partial^2 C_{\mathrm{SiO}}}{\partial z^2} = -f_1(T) C_{\mathrm{O}_2} C_{\mathrm{SiO}}, \tag{46b}$$

$$\frac{\partial T}{\partial t} - \frac{\partial^2 T}{\partial z^2} = h_1 f_1(T) C_{\mathrm{O}_2} C_{\mathrm{SiO}}. \tag{46c}$$

Defining the quantities $w_1(z,t) = C_{\mathrm{O}_2} - \frac{a}{2} C_{\mathrm{SiO}}$ and $w_2(z,t) = T + h_1 C_{\mathrm{SiO}}$, we find from (45)–(46) that

$$\frac{\partial w_1}{\partial t} - \frac{\partial^2 w_1}{\partial z^2} = 0, \quad w_1 \to 1 \quad \text{as} \quad z \to \infty, \quad w_1 \to -\frac{a}{2} \quad \text{as} \quad z \to -\infty, \tag{47a}$$

$$\frac{\partial w_2}{\partial t} - \frac{\partial^2 w_2}{\partial z^2} = 0, \quad w_2 \to 0 \quad \text{as} \quad z \to \infty, \quad w_2 \to 1 + h_1 \quad \text{as} \quad z \to -\infty. \tag{47b}$$

Solving (47) with appropriate Heaviside functions centered at $z = 0$ as initial data, we find

$$w_1(z,t) = \frac{1 + \mathrm{erf}(\eta)}{2} - \frac{a(1 - \mathrm{erf}(\eta))}{4} = \phi(\eta) - \frac{a}{2}\phi(-\eta), \tag{48a}$$

$$w_2(z,t) = (1 + h_1)\frac{1 - \mathrm{erf}(\eta)}{2} = (1 + h_1)\phi(-\eta), \tag{48b}$$

where $\eta = \frac{z}{2\sqrt{t}}$ is the similarity variable and $\phi(\eta) = \frac{1}{2}(1 + \mathrm{erf}(\eta))$. From the definitions of w_1 and w_2, we determine that

$$C_{\mathrm{O}_2} = \phi(\eta) - \frac{a}{2}\left(\phi(-\eta) - C_{\mathrm{SiO}}\right) \quad \text{and} \quad T = \phi(-\eta) + h_1\left(\phi(-\eta) - C_{\mathrm{SiO}}\right). \tag{49}$$

We now search for a solution of the form $C_{\mathrm{SiO}}(z,t) = u(\eta,\tau)$, $\eta = \frac{z}{2\sqrt{t}}$, $\tau = t$, and using (49), this puts (46b) into the form

$$\frac{\partial u}{\partial \tau} - \frac{1}{4\tau}\left(\frac{\partial^2 u}{\partial \eta^2} + 2\eta\frac{\partial u}{\partial \eta}\right) = -f_1\left(\phi(-\eta) + h_1\left(\phi(-\eta) - u\right)\right)\left(\phi(\eta) - \frac{a}{2}\left(\phi(-\eta) - u\right)\right)u. \tag{50}$$

In the small time limit $\tau \to 0^+$, a solution is possible only if

$$\frac{\partial^2 u}{\partial \eta^2} + 2\eta\frac{\partial u}{\partial \eta} = 0 \quad \text{as} \quad \tau \to 0^+, \tag{51}$$

and using the conditions (45), we find that $u \sim \Phi(-\eta)$ as $\tau \to 0^+$, that is, $C_{\mathrm{SiO}}(z,t) \sim \phi(-\frac{z}{2\sqrt{t}})$, $C_{\mathrm{O}_2} \sim \phi(\frac{z}{2\sqrt{t}})$, and $T \sim \phi(-\frac{z}{2\sqrt{t}})$ as $t \to 0^+$. Thus the heat and mass transfer mechanism is diffusion away from the initial conditions.

In the long time limit $\tau \to \infty$, we must resolve a moving front which corresponds to the reaction zone. Motivated in part by the application of similar approaches to other reaction-diffusion systems in the literature [5, 8, 9, 15], we consider a WKB approximation in order to resolve the sharp front, taking the ansatz $u(\eta,\tau) = \exp(-v(\eta,\tau))$, with $v(\eta,\tau) = \mathcal{O}(\tau^\beta)$ for some $\beta > 0$ to be determined. As the phase term v grows, localized rapid decay of the exponential results in a moving front. Using the WKB ansatz in (50), and neglecting the small parameter a (as we did in section 3.1.3), (50) becomes

$$\frac{\partial v}{\partial \tau} + \frac{1}{4\tau}\left(\left(\frac{\partial v}{\partial \eta}\right)^2 - \frac{\partial^2 v}{\partial \eta^2} - 2\eta\frac{\partial v}{\partial \eta}\right) = f_1\left((1+h_1)\phi(-\eta)\right)\phi(\eta) + \mathcal{R}, \tag{52}$$

where the error term $\mathcal{R} = [f_1((1+h_1)\phi(-\eta) - h_1 u) - f_1((1+h_1)\phi(-\eta))]\phi(\eta)$ results from omitting the explicit dependence of u in the argument of f_1 term given in (50). We expand v as

$$v(\eta,\tau) = \tau^\beta \sum_{\ell=0}^{\infty} \tau^{-\beta\ell} V_\ell(\eta) \quad \text{as} \quad \tau \to \infty, \tag{53}$$

and placing this into (52), we obtain the dominant balances which determine β: the time derivative term is $\mathcal{O}(\tau^{\beta-1})$, the dominant diffusion term is $\mathcal{O}(\tau^{2\beta-1})$, and the reaction term is $\mathcal{O}(\tau^0)$. Of the three possibilities, only the balance between the dominant diffusion term and the reaction kinetics is consistent with our assumptions and gives a value of $\beta > 0$. Taking the resulting $\beta = 1/2$ and placing (53) into (52), we find

$$\begin{aligned}\frac{1}{4}\left(\frac{dV_0}{d\eta}\right)^2 + \frac{\tau^{-1/2}}{2}\left(V_0 - \eta\frac{dV_0}{d\eta} - \frac{1}{2}\frac{d^2V_0}{d\eta^2} + \frac{dV_0}{d\eta}\frac{dV_1}{d\eta}\right) + \mathcal{O}(\tau^{-1}) \\ = f_1\left((1+h_1)\phi(-\eta)\right)\phi(\eta) + \mathcal{R}.\end{aligned} \tag{54}$$

Within the reaction zone, $u = \mathcal{O}(e^{-\sqrt{\tau}})$ and $\eta = \mathcal{O}(1)$. Since f_1 in (15) is positive and bounded with bounded derivative, there exists $\mathcal{O}(1)$ constant $R_0 > 0$ such that $|\mathcal{R}| < R_0\phi(\eta)u = \mathcal{O}(e^{-\sqrt{\tau}})$, and hence $\mathcal{R}$ is exponentially small within the reaction zone. To the left of the reaction zone, $u = \mathcal{O}(1)$ and $\eta \gg 1$. In this region, $\phi(\eta) < e^{-\eta^2}$ while $0 \le u \le \phi(-\eta) \le 1$, so $|\mathcal{R}| < [f_1(1+h_1) - f_1(0)]e^{-\eta^2} = \mathcal{O}(e^{-\eta^2})$, and hence $\mathcal{R}$ is exponentially small in this region, as well. As the expansion (53) is algebraic, the exponentially small term $\mathcal{R}$ is subdominant at each order in the expansion (53) and can be ignored when solving (54).

At leading order, $\mathcal{O}(1)$, we see that (54) gives

$$\frac{1}{4}\left(\frac{dV_0}{d\eta}\right)^2 = f_1\left((1+h_1)\phi(-\eta)\right)\phi(\eta). \tag{55}$$

Solving for V_0 and taking the positive root (so that the expansion in the WKB ansatz gives decay rather than blow-up at large time), we find

$$V_0(\eta) = 2\int_{-\infty}^{\eta-\eta_0} \sqrt{f_1\left((1+h_1)\phi(-\sigma)\right)\phi(\sigma)}\,d\sigma. \tag{56}$$

Since information about the initial configuration is lost in this long time limit, we have taken $\eta - \eta_0$ as the upper limit of the integral (56). Exploiting such a shift in the similarity variable can prove useful, and for our purposes we will use it to calibrate the large-time asymptotics to numerical simulations of the exact solution.

We then have $u(\eta,\tau) = \exp\left(-\tau^{1/2}V_0(\eta) + \mathcal{O}(1)\right)$ as $\tau \to \infty$. For large yet finite τ, $\lim_{\eta\to-\infty} u = 1$ while $\lim_{\eta\to\infty} u = 0$, in agreement with the boundary conditions on C_{SiO}, so no additional scaling of u is required at leading order. The next order correction, $V_1(\eta)$, will slightly correct the core structure near the moving front, but we find agreement with numerics is already good at leading order and omit higher order terms for the sake of brevity. Having determined the large-time asymptotics for C_{SiO}, we construct an approximate solution for (46),

$$
\begin{aligned}
&C_{\mathrm{SiO}}(z,t) \sim \exp\left(-\sqrt{t}V_0\left(\frac{z}{2\sqrt{t}}\right)\right), \quad C_{\mathrm{O}_2}(z,t) \sim \phi\left(\frac{z}{2\sqrt{t}}\right), \quad \text{and} \\
&T(z,t) \sim \phi\left(-\frac{z}{2\sqrt{t}}\right)(1+h_1) - h_1 \exp\left(-\sqrt{t}V_0\left(\frac{z}{2\sqrt{t}}\right)\right) \quad \text{as} \quad t \to \infty.
\end{aligned} \tag{57}
$$

The latter two quantities follow from (49) and the fact that the temperature depends on both diffusion and a source which involves the asymptotic solution for C_{SiO}. We solve the initial-boundary value problem (46) numerically by the method of lines, discretizing the PDEs in space and integrating the resulting ODEs in time. We use appropriate Heaviside functions centered at the origin as initial data in the numerics. As there will in general be an offset in the large-time asymptotics as large time expansions neglect initial data, we calibrate the asymptotics to the simulations by choosing η_0 to match both the asymptotic solution and the numerics at the unique value of z where $C_{\mathrm{SiO}} = 0.5$ for $t = 100$, finding $\eta_0 = 0.32$. In Figure 8 we compare both the asymptotic solution (solid lines) and the numerical result (dashed lines), showing that the agreement between the two solutions remains good as time increases.

We observe the reaction front moving to the left as SiO is being consumed by the combustion reaction with the much more plentiful ($a \ll 1$) oxygen. Due to its relative abundance, the oxygen slowly spreads due to diffusion, with a relatively small proportion of the oxygen reacting with SiO. The temperature behind the reaction front grows rapidly over time due to the combustion reaction, before leveling off to $T \sim 1 + h_1$ within the core region as the reaction slows. The hot reaction zone broadens as the front moves toward the left, with much of the new reactions between SiO and oxygen occurring near the front.

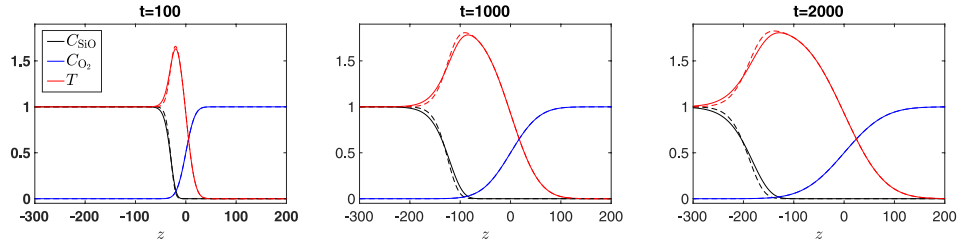

FIG. 8. *Plot of the approximate asymptotic solution* (57) *(solid lines) and numerical simulation (dashed lines) for SiO (black) and O_2 (blue) concentrations, and temperature (red), as indicated in the legend, from solving problem* (46).

4.2. Analytical solution of the particle density equation. As the parameter $d_p \approx 10^{-6}$, molecular diffusion is negligible relative to the chemical and thermal diffusivities in (18a), thus the resulting PDE is equivalent to (21a). Therefore, the analytical solution is similar to the one found for the case of initially well-mixed chemical species, but with an additional z dependence arising from the spatial variations in $C_{\mathrm{SiO_2}}$ and T. Let $C_{\mathrm{SiO_2}}(z, t_{\min}(z)) = C_{\mathrm{sat}}$; then the solution is given by

$$n = \frac{J(z,t_1)}{G(z,t_1)} \quad \text{with} \quad s = 1 + G^* \int_{t_1}^{t} G(z,\tau)\mathrm{d}\tau, \quad t_1 > t_{\min}(z), \tag{58}$$

for $t > t_{\min}(z)$. The solution is $n = 0$ for $t \le t_{\min}(z)$. Notice that in this case we need to be careful with the domain of definition of the solution since the value of $t_{\min}$ depends on z.

4.3. Numerical solution of the fully coupled model for $\zeta_1, \zeta_2 > 0$. Similar to what was done in section 3.3 in the well-mixed case, we solve the system (14) for initially separated initial data numerically and then use these results in the analytical solution for n found in section 4.2. We follow the same numerical scheme outlined at the end of section 4.1, that is, the method of lines. This method involves discretizing all PDEs in (14) in space while leaving the time variable continuous, which leads to a larger system of ODEs that is then numerically integrated in time. We plot numerical solutions for $C_{\mathrm{SiO_2}}$ and T in Figure 9 for both $\zeta_1 = \zeta_2 = 0$ (left) and $\zeta_1, \zeta_2 > 0$

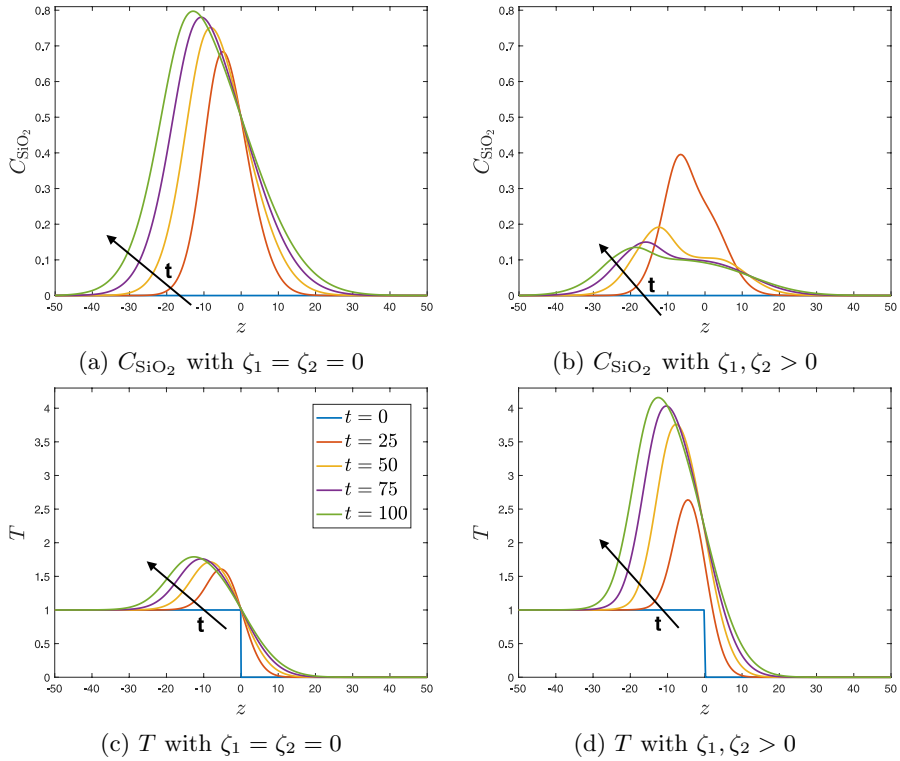

(a) $C_{\mathrm{SiO_2}}$ with $\zeta_1 = \zeta_2 = 0$ (b) $C_{\mathrm{SiO_2}}$ with $\zeta_1, \zeta_2 > 0$

(c) T with $\zeta_1 = \zeta_2 = 0$ (d) T with $\zeta_1, \zeta_2 > 0$

FIG. 9. (a), (b) *Concentration of* SiO_2 (C_{SiO_2}) *and* (c), (d) *temperature variations in* z, *for different times equally spaced from* $t = 0$ *to* 100 *as shown in the legend in* (c). *This is for the case* $\zeta_1 = \zeta_2 = 0$ *in* (a), (c) *and* $\zeta_1, \zeta_2 > 0$ *in* (b), (d). *We choose* $a = 0.2$, $C_{sat} = 0.1$, *with all other parameters as given in Table* 2.

(right), comparing each side-by-side at different values of time. In both cases there is initially zero concentration of SiO_2, and after a critical time the concentration increases and starts spreading slightly toward the left since it forms from the reaction between O_2 and SiO, moving left with the reaction region as shown in Figure 8. In the case of $\zeta_1, \zeta_2 > 0$, where we include a sink of SiO_2 due to the particle formation (Figure 9(b)), the concentration of SiO_2 decreases after time, since C_{SiO_2} is used up and rate limiting. In both cases the temperature increases with time; however, when $\zeta_1, \zeta_2 > 0$, heat is released during the particle formation process, and the extent of the temperature increase within the reaction zone is much greater. Therefore, although the asymptotic solutions are reasonable for a qualitative understanding of the dynamics, including the coupling of the particle growth back into the chemical-temperature system, $(\zeta_1, \zeta_2 > 0)$ is needed for quantitative accuracy, and to determine how fast SiO_2 is used in particle formation and growth. One can therefore view the $\zeta_1 = \zeta_2 = 0$ limit as modeling a situation where there is plentiful SiO_2 which is never used up due to a slow rate of particle growth, whereas the case of $\zeta_1, \zeta_2 > 0$ models the situation where SiO_2 is strongly rate limited and is used up in particle growth more rapidly than it is produced in the reaction zone.

To better understand properties of the particle distribution, n, we use the numerical solution for the chemistry-temperature system in the analytical formula (58) for n and plot J^*n over s and z for various time values in Figure 10. The largest particles (largest s) are located in the center of the reaction zone (as they have had time to grow), whereas smaller, newly formed particles are located near the boundary of the zone. The region with particles $(n > 0)$ grows in spatial extent with the reaction zone, and the highest density of particles is at the boundary near the reaction front. In the case where there is coupling of the particle growth back into the chemistry-temperature system, $\zeta_1, \zeta_2 > 0$, we observe a resurgence of small particles being formed over the entire reaction zone, rather than just near the boundary (see lower right panel of Figure 10). We hypothesize that this originates from the comparatively high temperatures arising in the fully coupled system, which results in the last of the SiO_2 being used up to rapidly make smaller particles, after which point the process ends as SiO_2 is depleted, with these particles growing no further. Our theoretical results showing a build-up of smaller particles (in addition to the existing larger particles) are in agreement with earlier experimental findings [26].

The mean and variance of the particle distribution are shown in Figure 11. The mean size of the particles, as well as their variance, is larger when $\zeta_1, \zeta_2 = 0$, since in this case there is more SiO_2 produced than is used in particle formation. This is also apparent from Figure 10. In contrast, when $\zeta_1, \zeta_2 > 0$, the SiO_2 is used in finite time, hence there is less material available for particle growth, and smaller particles result. Panels on the right-hand side of Figure 11 are akin to spatial generalizations of the well-mixed case shown in Figure 5(e).

5. Discussion. Motivated by microsilica particle formation inside a silicon furnace hood, we derived a mathematical model consisting of a heat and mass transfer system associated with two dominant chemical reactions taking place within the furnace coupled to a population balance equation for microsilica particle formation and growth. The material consumed and heat released due to particle formation was also coupled back to the relevant mass and energy conservation equations. After simplifying the geometry, we studied a one-dimensional model in space for the dynamics near, within, and around the reaction zone or flame. Making a variety of simplifying assumptions and considering various cases for the coupling of particle growth with

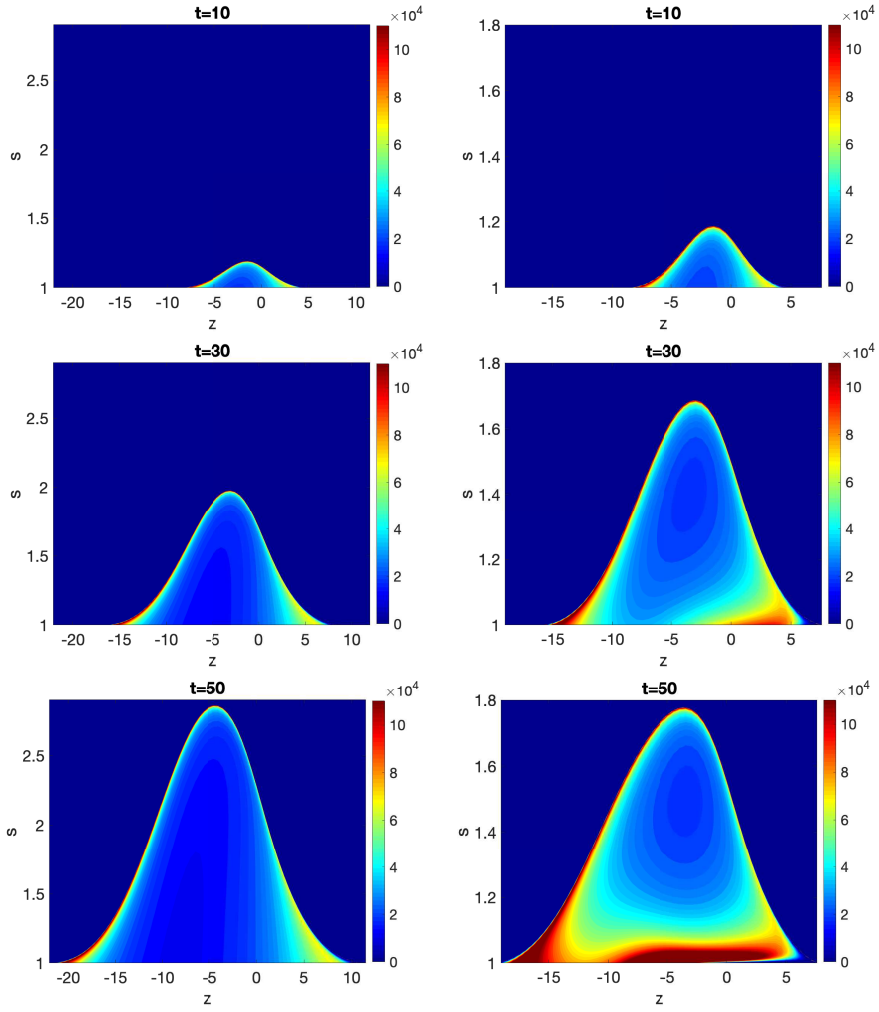

FIG. 10. *Heat maps for J^*n with respect to s and z, for different values of time. This is for the case $\zeta_1 = \zeta_2 = 0$ (left) and $\zeta_1, \zeta_2 > 0$ (right). We choose $a = 0.2$, $C_{sat} = 0.1$, with all other parameters as given in Table 2.*

the heat and mass transfer system, we arrived at an assortment of asymptotic and numerical results which give insight into the physical processes resulting in microsilica formation.

We first considered a configuration where the chemical species are well-mixed, and hence diffusion plays no role, with this case modeling dynamics most valid on a small lengthscale within the reaction zone. In the case where the mass and energy equations are coupled into the particle growth equation, but not the other way around ($\zeta_1 = \zeta_2 = 0$), we obtained asymptotic solutions for small a, that is, for an oxygen rich environment (which is the physically relevant limit), and these compared favorably with numerical simulations. The SiO reaction occurs much faster than the CO reaction, and if enough oxygen is available, all of the initial SiO will be consumed, hence the same number of moles of SiO_2 will be produced. As the sink term in the mass conservation was neglected, particles continued to grow since the particle mass was negligible to the total mass of SiO_2 remaining. However, when the particle growth

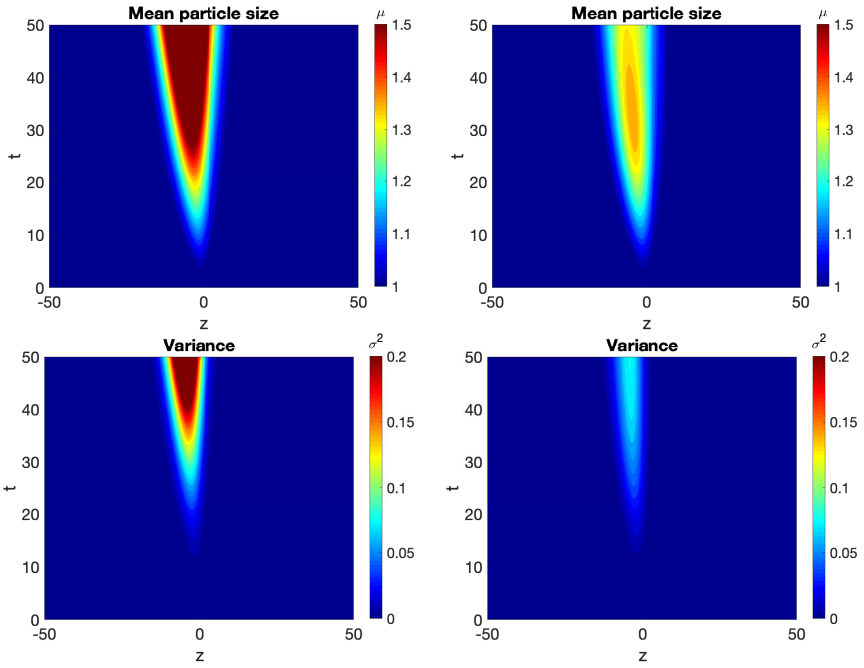

FIG. 11. *Heat maps for μ and σ^2 from top to bottom with respect to t and z. The figures on the left are for the case $\zeta_1 = \zeta_2 = 0$ and the ones on the right for $\zeta_1, \zeta_2 > 0$. We choose $a = 0.2$, $C_{sat} = 0.1$, with all other parameters as given in Table 2.*

process was coupled back to the mass and energy conservation ($\zeta_1, \zeta_2 > 0$ in which case only numerical simulations were possible), we observed that the number and size of particles formed was limited, with particle growth ending once the mass of SiO_2 was depleted. Therefore, the asymptotics obtained for $\zeta_1 = \zeta_2 = 0$ and $a \ll 1$ are most useful either for understanding early-time dynamics (before SiO_2 is depleted due to particle formation and growth) or in the regime where O_2 is plentiful, and the rate of depletion of SiO_2 is small (i.e., when the reaction R_1 in (1) produces a sufficiently large quantity of SiO_2 so that it is not depleted rapidly by the sink term (10)). The sink term (10) therefore sets the timescale for the fully coupled system. An additional finding was that our solutions result in a bimodal size distribution of microsilica particles, with a submicron range of particle sizes containing most of the particle mass, and a micron range with fewer but much larger particles, and this finding is consistent with experimental results present in the literature [10].

In the second configuration that we studied, the chemical species are initially spatially separated, with O_2 plentiful on one side of the domain and the other chemical species plentiful on the other side of the domain. Given an initial temperature distribution characteristic of what is found in a cross section of a furnace, reactions occur within a narrow reaction zone. As O_2 is the most plentiful of the reactants, the reaction zone will propagate toward the other fuel components through diffusion. We observe that the dynamics within the core of the reaction zone are indeed similar to those of the spatially well-mixed case, verifying our intuition that the well-mixed case is indeed a simple yet effective representation of the dynamics within the flame. The longest-lived and largest particles arise in the center of the reaction zone, where SiO_2 is most abundant, and these match best with the predictions from the well-mixed

limit. Meanwhile, the full spatial model is useful for better understanding the distribution of particles sizes over space and time, with gradually smaller particles being produced toward the boundary of the reaction zone.

We conclude that O_2 availability and a sufficiently high temperature are essential for the combustion reactions to occur, strongly influencing both the width of the reaction zone and the particle size distribution. A decrease in the availability of O_2 results in a more narrow reaction zone and hence limits SiO_2 production over a given time interval. Regarding industrial scale processes which motivate our work, this finding suggests operators to provide adequate inflow of O_2, particularly if larger SiO_2 particles are sought. In addition, we find that increasing the saturation or equilibrium concentration of SiO_2 (for instance, by decreasing T) will result in a decrease in mean particle size, although this parameter depends on other environmental factors, and may be more challenging to control in practical applications.

Our work provides a qualitative underlying of the physical processes at play when microsilica is produced, yet in order to improve the quantitative agreement with experiments and real-world furnace observations, there are some extensions to consider in future work. The most immediate extension is to couple the model we have developed to a momentum equation for the flow of gas within the furnace. While we have considered the velocity to be uniform, and hence scaled it out of the problem, the fluid problem is in practice more dynamic, with preliminary simulations suggesting the emergence of eddies and related localized structures, which may trap particles, allowing them to recirculate through reaction zones multiple times before they are ejected from the furnace through the exhaust pipe. In related applications, microscopic zones where individual particles grow may be several orders of magnitude smaller than macroscopic turbulent eddies [40], with the reaction zones highly localized within the turbulent flow. This suggests that the narrow reaction zones we study will likely still exist within the larger flow, embedded within boundary layers formed near the interface of O_2 and SiO. There is recent work modeling fine-particle formation in turbulent flames [29], large-scale simulation of aerosol nucleation and growth in turbulent mixing layers [44], with Favre-averaged population balance equations being used in many cases [45], and some of these approaches may prove useful. More complex and realistic geometries for the furnace should also be considered, since the geometry of the problem domain will influence the flow problem, even if domain geometry does not strongly modify dynamics within the reaction zone, which is orders of magnitude smaller.

REFERENCES

[1] D. Alexandrov, *Nucleation and crystal growth in binary systems*, J. Phys. A, 47 (2014), 125102.

[2] A. Anikin, G. Galevsky, V. Rudneva, E. Nozdrin, and S. Galevsky, *Development of scientific and technological bases for application of brown coal semi coke in the technology of non-milled silicon carbide*, in IOP Conference Series: Materials Science and Engineering, vol. 150, IOP Publishing, 2016, p. 012005.

[3] C. Artelt, H.-J. Schmid, and W. Peukert, *Modelling titania formation at typical industrial process conditions: Effect of surface shielding and surface energy on relevant growth mechanisms*, Chemical Engineering Science, 61 (2006), pp. 18–32.

[4] A. Bermúdez, J. L. Ferrín, and S. A. Halvorsen, *Process Models for the Production of Microalumina*, Tech. report, 97 European Study Group with Industry, Santiago de Compostela, 2013.

[5] E. Bouin, V. Calvez, N. Meunier, S. Mirrahimi, B. Perthame, G. Raoul, and R. Voituriez, *Invasion fronts with variable motility: Phenotype selection, spatial sorting and wave acceleration*, C. R. Math., 350 (2012), pp. 761–766.

[6] F. Brosa Planella, C. P. Please, and R. A. Van Gorder, *Extended Stefan problem for solidification of binary alloys in a finite planar domain*, SIAM J. Appl. Math., 79 (2019), pp. 876–913.
[7] J. Buckmaster, *The Mathematics of Combustion*, Frontiers in Appl. Math., SIAM, Philadelphia, 1985.
[8] D. S. Cohen, F. C. Hoppensteadt, and R. M. Miura, *Slowly modulated oscillations in nonlinear diffusion processes*, SIAM J. Appl. Math., 33 (1977), pp. 217–229.
[9] C. Cuesta and J. King, *Front propagation in a heterogeneous Fisher equation: the homogeneous case is non-generic*, Quart. J. Mech. Appl. Math., 63 (2010), pp. 521–571.
[10] E. Dingsøyr, M. Dåstøl, and W. Wedberg, *Particle size and particle size distribution of Elkem microsilica and its relevance to technical application*, in Proceedings of the 5th European Symposium on Particle Characterization, Nurnberg, Germany, 1992, pp. 24–26.
[11] *Personal communication*, Elkem ASA.
[12] R. C. Flagan and M. M. Lunden, *Particle structure control in nanoparticle synthesis from the vapor phase*, Materials Sci. Engrg. A, 204 (1995), pp. 113–124.
[13] R. C. Flagan and J. H. Seinfeld, *Fundamentals of Air Pollution Engineering*, Courier Corporation, Chelmsford, MA, 2012.
[14] S. Halvorsen, *A unidimensional dynamic model for the(ferro) silicon process*, in Electric Furnace Conference Proceedings, Vol. 50, 1992, pp. 45–59.
[15] L. N. Howard and N. Kopell, *Slowly varying waves and shock structures in reaction-diffusion equations*, Stud. Appl. Math., 56 (1977), pp. 95–145.
[16] M. Kadkhodabeigi, H. Tveit, and K. Berget, *Silicon process-new hood design for tapping gas collection*, in Proceedings of the 12th International Ferroalloys Congress, 2010, pp. 109–119.
[17] N. E. Kamfjord, *Mass and Energy Balances of the Silicon Process—Improved Emission Standards*, Ph.D. thesis, Norwegian University of Science and Technology, 2012.
[18] D. Krause and H. Loch, *Mathematical Simulation in Glass Technology*, Springer, New York, 2012.
[19] B. Lee, J. Jeong, J. Hwang, M. Choi, and S. Chung, *Analysis of growth of non-spherical silica particles in a counterflow diffusion flame considering chemical reactions, coagulation and coalescence*, J. Aerosol Sci., 32 (2001), pp. 165–185.
[20] H. Lim, T. Kim, S. Eom, Y.-i. Sung, M. Moon, and D. Lee, *Vaporization process of SiO2 particles for slurry injection in inductively coupled plasma atomic emission spectrometry*, J. Anal. Atomic Spectrometry, 17 (2002), pp. 109–114.
[21] J. Lothe and G. M. Pound, *Reconsiderations of nucleation theory*, J. Chem. Phys., 36 (1962), pp. 2080–2085.
[22] B. Lund, B. Foss, K. Løvåsen, and B. Ydstie, *Sensitivity analysis of a dynamic model for submerged arc silicon furnaces*, in Proceedings of the 10th International Ferroalloys Congress, Vol. 1, 2004.
[23] E. V. Makoveeva and D. V. Alexandrov, *A complete analytical solution of the Fokker–Planck and balance equations for nucleation and growth of crystals*, Philos. Trans. A, 376 (2018), 20170327.
[24] W. Massman, *A review of the molecular diffusivities of H2O, CO2, CH4, CO, O3, SO2, NH3, N2O, NO, and NO2 in air, O2 and N2 near STP*, Atmos. Environ., 32 (1998), pp. 1111–1127.
[25] M. K. Næss, *Mechanisms and Kinetics of Liquid Silicon Oxidation*, Ph.D. thesis, Norwegian University of Science and Technology, 2013.
[26] M. K. Næss, G. Tranell, J. E. Olsen, N. E. Kamfjord, and K. Tang, *Mechanisms and kinetics of liquid silicon oxidation during industrial refining*, Oxidation Metals, 78 (2012), pp. 239–251.
[27] K. Okuyama, Y. Kousaka, D. R. Warren, R. C. Flagan, and J. H. Seinfeld, *Homogeneous nucleation by continuous mixing of high temperature vapor with room temperature gas*, Aerosol Sci. Technol., 6 (1987), pp. 15–27.
[28] S. E. Pratsinis, *Simultaneous nucleation, condensation, and coagulation in aerosol reactors*, J. Colloid Interface Sci., 124 (1988), pp. 416–427.
[29] V. Raman and R. O. Fox, *Modeling of fine-particle formation in turbulent flames*, Annu. Rev. Fluid Mech., 48 (2016), pp. 159–190.
[30] D. Ramkrishna, *Population Balances: Theory and Applications to Particulate Systems in Engineering*, Elsevier, Amsterdam, 2000.
[31] A. Schei, J. K. Tuset, and H. Tveit, *Production of High Silicon Alloys*, Tapir Trondheim, Norway, 1998.
[32] T. Seto, A. Hirota, T. Fujimoto, M. Shimada, and K. Okuyama, *Sintering of polydisperse nanometer-sized agglomerates*, Aerosol Sci. Technol., 27 (1997), pp. 422–438.

[33] S. Shekar, A. J. Smith, W. J. Menz, M. Sander, and M. Kraft, *A multidimensional population balance model to describe the aerosol synthesis of silica nanoparticles*, J. Aerosol Sci., 44 (2012), pp. 83–98.
[34] B. M. Sloman, C. P. Please, and R. A. Van Gorder, *Asymptotic analysis of a silicon furnace model*, SIAM J. Appl. Math., 78 (2018), pp. 1174–1205.
[35] B. M. Sloman, C. P. Please, R. A. Van Gorder, A. M. Valderhaug, R. G. Birkeland, and H. Wegge, *A heat and mass transfer model of a silicon pilot furnace*, Metallurgical Materials Trans. B, 48 (2017), pp. 2664–2676.
[36] B. M. Smirnov, *Nanoclusters and Microparticles in Gases and Vapors*, De Gruyter Stud. Math. Phys. 6, Walter de Gruyter, Berlin, 2012.
[37] S. Stankic, M. Cottura, D. Demaille, C. Noguera, and J. Jupille, *Nucleation and growth concepts applied to the formation of a stoichiometric compound in a gas phase: The case of MGO smoke*, J. Crystal Growth, 329 (2011), pp. 52–56.
[38] W. Tsang and R. Hampson, *Chemical kinetic data base for combustion chemistry. Part I. Methane and related compounds*, J. Phys. Chemical Reference Data, 15 (1986), pp. 1087–1279.
[39] S. R. Turns, *An Introduction to Combustion: Concepts and Applications*, 2nd ed., McGraw-Hill, New York, 2000.
[40] G. D. Ulrich, *Theory of particle formation and growth in oxide synthesis flames*, Combustion Sci. Technol., 4 (1971), pp. 47–57.
[41] P. K. Wang, *Physics and Dynamics of Clouds and Precipitation*, Cambridge University Press, Cambridge, UK, 2013.
[42] D. R. Warren and J. H. Seinfeld, *Prediction of aerosol concentrations resulting from a burst of nucleation*, J. Colloid Interface Sci., 105 (1985), pp. 136–142.
[43] F. A. Williams, *Combustion Theory*, CRC Press, Boca Raton, FL, 2018.
[44] K. Zhou, A. Attili, A. Alshaarawi, and F. Bisetti, *Simulation of aerosol nucleation and growth in a turbulent mixing layer*, Phys. Fluids, 26 (2014), 065106.
[45] A. Zucca, D. L. Marchisio, A. A. Barresi, and R. O. Fox, *Implementation of the population balance equation in CFD codes for modelling soot formation in turbulent flames*, Chem. Engrg. Sci., 61 (2006), pp. 87–95.